

The North Atlantic Waveguide and Downstream Impact Experiment

Article

Accepted Version

Creative Commons: Attribution 4.0 (CC-BY)

Schäfler, A., Craig, G., Wernli, H., Arbogast, P., Doyle, J. D., McTaggart-Cowan, R., Methven, J., Rivière, G., Ament, F., Boettcher, M., Bramberger, M., Cazenave, Q., Cotton, R., Crewell, S., Delanoë, J., Dörnbrack, A., Ehrlich, A., Ewald, F., Fix, A., Grams, C. M., Gray, S. L., Grob, H., Groß, S., Hagen, M., Harvey, B., Hirsch, L., Jacob, M., Kölling, T., Konow, H., Lemmerz, C., Lux, O., Magnusson, L., Mayer, B., Mech, M., Moore, R., Pelon, J., Quinting, J., Rahm, S., Rapp, M., Rautenhaus, M., Reitebuch, O., Reynolds, C. A., Sodemann, H., Spengler, T., Vaughan, G., Wendisch, M., Wirth, M., Witschas, B., Wolf, K. and Zinner, T. (2018) The North Atlantic Waveguide and Downstream Impact Experiment. *Bulletin of the American Meteorological Society*, 99 (8). pp. 1607-1637. ISSN 1520-0477 doi: <https://doi.org/10.1175/BAMS-D-17-0003.1> Available at <http://centaur.reading.ac.uk/76719/>

It is advisable to refer to the publisher's version if you intend to cite from the work.

To link to this article DOI: <http://dx.doi.org/10.1175/BAMS-D-17-0003.1>

Publisher: American Meteorological Society

All outputs in CentAUR are protected by Intellectual Property Rights law, including copyright law. Copyright and IPR is retained by the creators or other copyright holders. Terms and conditions for use of this material are defined in the [End User Agreement](#).

www.reading.ac.uk/centaur

CentAUR

Central Archive at the University of Reading

Reading's research outputs online



AMERICAN METEOROLOGICAL SOCIETY

Bulletin of the American Meteorological Society

EARLY ONLINE RELEASE

This is a preliminary PDF of the author-produced manuscript that has been peer-reviewed and accepted for publication. Since it is being posted so soon after acceptance, it has not yet been copyedited, formatted, or processed by AMS Publications. This preliminary version of the manuscript may be downloaded, distributed, and cited, but please be aware that there will be visual differences and possibly some content differences between this version and the final published version.

The DOI for this manuscript is doi: 10.1175/BAMS-D-17-0003.1

The final published version of this manuscript will replace the preliminary version at the above DOI once it is available.

If you would like to cite this EOR in a separate work, please use the following full citation:

Schäfler, A., G. Craig, H. Wernli, P. Arbogast, J. Doyle, R. McTaggart-Cowan, J. Methven, G. Rivière, F. Ament, M. Boettcher, M. Bramberger, Q. Cazenave, R. Cotton, S. Crewell, J. Delanoë, A. Dörnbrack, A. Ehrlich, F. Ewald, A. Fix, C. Grams, S. Gray, H. Grob, S. Groß, M. Hagen, B. Harvey, L. Hirsch, M. Jacob, T. Kölling, H. Konow, C. Lemmerz, O. Lux, L. Magnusson, B. Mayer, M. Mech, R. Moore, J. Pelon, J. Quinting, S. Rahm, M. Rapp, M. Rautenhaus, O. Reitebuch, C. Reynolds, H. Sodemann, T. Spengler, G. Vaughan, M. Wendisch, M. Wirth, B. Witschas, K. Wolf, and T. Zinner, 2018: The North Atlantic Waveguide and Downstream Impact Experiment. *Bull. Amer. Meteor. Soc.* doi:10.1175/BAMS-D-17-0003.1, in press.



1 **The North Atlantic Waveguide and Downstream Impact Experiment**

2 Andreas Schäfler, George Craig, Heini Wernli, Philippe Arbogast, James D. Doyle,
3 Ron McTaggart-Cowan, John Methven, Gwendal Rivière, Felix Ament, Maxi Boettcher,
4 Martina Bramberger, Quitterie Cazenave, Richard Cotton, Susanne Crewell, Julien Delanoë,
5 Andreas Dörnbrack, André Ehrlich, Florian Ewald, Andreas Fix, Christian M. Grams,
6 Suzanne L. Gray, Hans Grob, Silke Groß, Martin Hagen, Ben Harvey, Lutz Hirsch, Marek Jacob,
7 Tobias Kölling, Heike Konow, Christian Lemmerz, Oliver Lux, Linus Magnusson, Bernhard Mayer,
8 Mario Mech, Richard Moore, Jacques Pelon, Julian Quinting, Stephan Rahm, Markus Rapp,
9 Marc Rautenhaus, Oliver Reitebuch, Carolyn A. Reynolds, Harald Sodemann, Thomas Spengler,
10 Geraint Vaughan, Manfred Wendisch, Martin Wirth, Benjamin Witschas, Kevin Wolf, Tobias Zinner

11 **Affiliations:** SCHÄFLER, BRAMBERGER, DÖRNBRACK, EWALD, FIX, GROß, HAGEN,
12 LEMMERZ, LUX, RAHM, RAPP, REITEBUCH, WIRTH AND WITSCHAS — Deutsches Zentrum
13 für Luft- und Raumfahrt, Oberpfaffenhofen, Germany; CRAIG, GROB, KÖLLING, MAYER AND
14 ZINNER — Ludwig-Maximilians-Universität, München, Germany; BOETTCHER, GRAMS AND
15 WERNLI — ETH Zürich, Switzerland; ARBOGAST — CNRM, Météo-France/CNRS, Toulouse,
16 France; DOYLE AND REYNOLDS — Naval Research Laboratory, Monterey, California;
17 MCTAGGART-COWAN — Environment and Climate Change Canada, Dorval, Canada; GRAY,
18 HARVEY AND METHVEN — Department of Meteorology, University of Reading, Reading, United
19 Kingdom, UK; RIVIÈRE — LMD/IPSL, ENS/PSL Research University/CNRS, Paris, France;
20 CREWELL, JACOB AND MECH — Universität Köln, Köln, Germany; CAZENAVE, DELANOË
21 AND PELON — Laboratoire ATmosphère, Milieux, et Observations Spatiales (LATMOS),
22 Guyancourt, France; COTTON — Met Office, Exeter, United Kingdom; EHRLICH, WENDISCH
23 AND WOLF — Universität Leipzig, Leipzig, Germany; HIRSCH — Max Planck Institute for
24 Meteorology, Hamburg, Germany; AMENT AND KONOW — Universität Hamburg, Hamburg,
25 Germany and Max Planck Institute for Meteorology, Hamburg, Germany; MAGNUSSON —
26 European Centre for Medium-Range Weather Forecasts, Reading, United Kingdom; MOORE —
27 Norwegian Meteorological Institute / University of Oslo, Oslo, Norway; QUINTING — ETH Zürich,
28 Switzerland and Monash University, Clayton, Australia; RAUTENHAUS — Technische Universität
29 München, Garching, Germany; SODEMANN AND SPENGLER — Geophysical Institute, University
30 of Bergen and Bjerknes Centre for Climate Research, Bergen, Norway; VAUGHAN — National
31 Centre for Atmospheric Science, University of Manchester, Manchester, United Kingdom

32 **Corresponding author:**

33 Dr. Andreas Schäfler, Institut für Physik der Atmosphäre, Deutsches Zentrum für Luft- und Raumfahrt
34 (DLR), Oberpfaffenhofen, 82234 Weßling, Germany, email: andreas.schäfler@dlr.de

35 **Capsule.** Multi-aircraft and ground-based observations were made over the North Atlantic in
36 fall 2016 to investigate the importance of diabatic processes for midlatitude weather.

37 **Abstract.** The North Atlantic Waveguide and Downstream Impact Experiment (NAWDEX)
38 explored the impact of diabatic processes on disturbances of the jet stream and their influence
39 on downstream high-impact weather through the deployment of four research aircraft, each
40 with a sophisticated set of remote-sensing and in situ instruments, and coordinated with a
41 suite of ground-based measurements. A total of 49 research flights were performed, including,
42 for the first time, coordinated flights of the four aircraft; the German High Altitude and Long
43 Range Research Aircraft (HALO), the Deutsches Zentrum für Luft- und Raumfahrt (DLR)
44 Dassault Falcon 20, the French Service des Avions Français Instrumentés pour la Recherche
45 en Environnement (SAFIRE) Falcon 20, and the British Facility for Airborne Atmospheric
46 Measurements (FAAM) BAe 146. The observation period from 17 Sep to 22 Oct 2016 with
47 frequently occurring extratropical and tropical cyclones was ideal to investigate midlatitude
48 weather over the North Atlantic. NAWDEX featured three sequences of upstream triggers of
49 waveguide disturbances, their dynamic interaction with the jet stream, subsequent
50 development, and eventual downstream weather impact on Europe. Examples are presented to
51 highlight the wealth of phenomena that were sampled, the comprehensive coverage and the
52 multi-faceted nature of the measurements. This unique dataset forms the basis for future case
53 studies and detailed evaluations of weather and climate predictions to improve our
54 understanding of diabatic influences on Rossby waves and downstream impact of weather
55 systems affecting Europe.

56 Progress in understanding the processes controlling midlatitude weather is one of the factors
57 that have contributed to a continuous improvement in the skill of medium-range weather
58 forecasts in recent decades (Thorpe 2004; Richardson et al. 2012; Bauer et al. 2015).
59 Additionally, numerical weather prediction (NWP) has undergone a revolution in recent
60 years, with the development and widespread use of ensemble prediction systems (EPS) to
61 represent forecast uncertainty (Bauer et al. 2015). However, the short-term prediction of high-
62 impact weather (HIW) events (e.g., strong winds and heavy precipitation), and the medium-
63 range prediction of extratropical cyclones, including their tracks and intensity, is still a major
64 challenge (e.g., Frame et al. 2015). Recent research on midlatitude weather has focused on
65 quantifying model errors and predictability, and in particular on investigating the role of
66 diabatic processes such as those related to clouds and radiation, whose interaction with the
67 dynamics of the flow must be understood and represented more accurately in models in order
68 to further improve forecast quality.

69 Detailed observations are needed to characterize the weather systems and embedded
70 physical processes across a range of spatial and temporal scales that encompass cloud
71 microphysical variability and Rossby waves. In September and October 2016, the North
72 Atlantic Waveguide and Downstream Impact Experiment (NAWDEX) made new multi-scale
73 observations in the North Atlantic basin from eastern Canada to western Europe. Weather
74 features expected to be associated with forecast errors were extensively probed, providing a
75 high-quality set of observations that are not assimilated routinely and thus can be used for
76 validation of the NWP systems.

77 The fall season was chosen for the experiment because diabatic processes are particularly
78 active due to relatively high sea surface temperatures and the jet stream is intensifying as the
79 high latitudes cool. Many of the weather phenomena central to the growth of disturbances on
80 the jet stream and midlatitude predictability are active in fall, such as extratropical cyclones
81 with intense fronts and warm conveyor belts (WCBs), carrying air from the oceanic boundary

82 layer into ridges at the tropopause level. There is also the possibility of North Atlantic tropical
83 cyclones (TCs) recurving poleward into midlatitudes and undergoing extratropical transition
84 (ET) – a process known to be associated with low predictability (Harr et al. 2008). Coherent
85 mesoscale depressions of the tropopause, known as tropopause polar vortices (TPVs, Cavallo
86 and Hakim 2010; Kew et al. 2010), can disturb the jet stream if they move equatorward from
87 the Arctic.

88 NAWDEX contributes to the World Weather Research Program (WWRP) and its High
89 Impact Weather project (Jones and Golding 2015), and aims to provide the observational
90 foundation for further investigating cloud diabatic processes and radiative transfer in North
91 Atlantic weather systems, which will form the basis for future improvements in the prediction
92 of HIW over Europe.

93 **THE ROLE OF DIABATIC PROCESSES.** Weather in Europe strongly depends on the
94 life-cycle of Rossby waves that propagate along the slowly varying part of the North Atlantic
95 jet stream (Martius et al. 2010). The strong meridional potential vorticity (PV) gradient
96 associated with the jet stream serves as a waveguide for propagating Rossby waves.
97 Frequently, small disturbances in the jet entrance region over eastern North America grow in
98 baroclinic weather systems and evolve into large-amplitude features in the European sector
99 (Schwierz et al. 2004). Figure 1 portrays an idealized North Atlantic flow situation that could
100 result in HIW in the form of high winds and heavy precipitation over northern Europe. In
101 addition to Rossby waves amplifying through baroclinic instability, diabatic processes are
102 able to modify upper-tropospheric PV at the level of the midlatitude jet stream, which impacts
103 the wavelength and amplitude of the downstream Rossby wave development (e.g., Massacand
104 et al. 2001; Knippertz and Martin 2005; Grams et al. 2011; Teubler and Riemer 2016).

105 The majority of precipitation and cloud diabatic processes in extratropical cyclones occur
106 within a coherent airstream known as the WCB. It carries warm, moist air from the low-level

107 warm sector of a cyclone to the ridge at tropopause level within 1-2 days (Browning et al.
108 1973; Carlson 1980; Wernli and Davies 1997). The boundary layer humidity in the inflow of
109 WCBs (Region 1 in Fig. 1) can impact the outflow height of WCBs (Schäfler and Harnisch
110 2015). For some WCBs, the inflow region coincides with a filament of strong horizontal
111 water vapor transport, a so-called “atmospheric river”, which can contribute to intense rain in
112 the midlatitudes (Lavers and Villarini 2013). During the ascent of WCBs (Region 2 in Fig. 1),
113 latent heating due to cloud microphysical processes, embedded convection and turbulent
114 fluxes influence the level of the outflow layer, the direction taken by outflow air masses, and
115 the shape of the upper-level ridge (Martínez-Alvarado et al. 2014; Joos and Forbes 2016). The
116 latent heating in WCBs is strong both in the early phase of the ascent when condensation
117 dominates and later when mixed-phase clouds are formed and vapor deposition on ice crystals
118 and snow becomes important (Joos and Wernli 2012).

119 The effect of the heating on the PV structure is to produce a positive PV anomaly in the
120 lower troposphere (Wernli and Davies 1997), which influences the structure and evolution of
121 midlatitude surface cyclones (e.g., Kuo et al. 1991; Davis et al. 1993; Binder et al. 2016).
122 Above the level of maximum latent heating, PV is reduced by cloud diabatic processes
123 leading to negative PV anomalies in the upper-tropospheric WCB outflow region (Wernli
124 1997; Pomroy and Thorpe 2000; Madonna et al. 2014; Methven 2015). The divergent outflow
125 winds (Region 3 in Fig. 1) tend to amplify the upper-level downstream ridge and to intensify
126 the jet stream by strengthening the PV gradient (Archambault et al. 2013). If the outflow layer
127 is higher, the negative PV anomaly is stronger and more air mass enters the anticyclonic
128 branch of the WCB flowing into the downstream ridge (Grams and Archambault 2016). In
129 addition, a sharp peak in longwave radiative cooling near the tropopause, associated with a
130 step change in water vapor, creates a reinforcement of the positive PV anomaly in upper-level
131 troughs (Chagnon et al. 2013) and plays a key role in maintaining and strengthening TPVs
132 (Cavallo and Hakim 2012).

133 Diabatic processes also play a key role in weather systems that act as triggers to disturb
134 the midlatitude waveguide. Recurving TCs undergoing ET (Jones et al. 2003) can enhance the
135 anticyclonic and divergent flow at upper levels, excite and amplify Rossby waves and cause
136 downstream forecast errors, as well as HIW events (e.g., Agusti-Panareda et al. 2004; Harr et
137 al. 2008; Riemer and Jones 2010). Radiatively maintained TPVs, which are positive PV
138 anomalies above the tropopause, can disturb the Rossby waveguide from polar latitudes.

139 Rossby wave breaking leads to PV filamentation, forming smaller-scale PV anomalies
140 such as PV streamers and cut-off vortices. They form frequently over the eastern North
141 Atlantic and Europe (e.g., Wernli and Sprenger 2007), and several studies have reported their
142 relevance for triggering HIW, in particular heavy precipitation (e.g., Martius et al. 2006;
143 Chaboureaud and Claud 2006; Grams and Blumer 2015). Synoptic wave breaking events are
144 also important for the large-scale flow itself as they reinforce weather regimes such as
145 blocking ridges (Michel and Rivière 2011; Spensberger and Spengler 2014). Blocks are also
146 strongly influenced by diabatic processes in air masses ascending from the lower troposphere
147 (Pfahl et al. 2015).

148 Disturbances of the waveguide and associated errors can amplify and propagate
149 downstream, and may cause significant forecast errors over Europe (Madonna et al. 2015;
150 Martínez-Alvarado et al. 2016) (Region 4 in Fig. 1). In NWP models, diabatic processes such
151 as those associated with convection, cloud microphysics and radiation are represented by
152 parameterizations of varying degrees of fidelity and may contain both systematic and random
153 errors that influence forecast skill. A distinct Rossby wave pattern associated with poleward
154 transport of warm and moist air over the eastern US and strong diabatic activity has been
155 identified as a common precursor 6 days before the worst forecast busts over Europe
156 (Rodwell et al. 2013). Upscale error growth experiments in numerical models show that the
157 growth of small-scale perturbations is initially confined to regions where condensation is
158 occurring, with the regions of large error amplitude gradually expanding to affect the

159 synoptic-scale weather pattern (Zhang et al. 2007; Selz and Craig 2015). Doyle et al. (2014)
160 found forecasts of an extratropical cyclone with severe impact in western Europe to be very
161 sensitive to the initial low-level moisture, which influenced the moisture supply in a WCB. At
162 upper levels, global NWP models fail to maintain a sufficiently sharp tropopause, showing a
163 decrease in sharpness with forecast lead time (Gray et al. 2014). This influence on the
164 waveguide can have major implications for the representation of the downstream propagation
165 and amplification of Rossby waves in NWP (Harvey et al. 2015) and the associated prediction
166 of HIW.

167 Previous studies using measurements to study the influence of diabatic processes on the
168 Rossby waveguide have been primarily based on routinely collected observations by
169 operational meteorological services. These observations rely largely on satellite data, which
170 models predominantly assimilate in cloud-free areas, and on sparse in situ measurements, all
171 of which are combined in the data assimilation system using model forecasts as a background
172 estimate. This approach to studying diabatic processes has significant limitations since these
173 processes tend to be strongest in cloudy and precipitating regions, which are particularly
174 challenging for both observation and modeling systems. The processes associated with
175 diabatic heating are characterized by a high-degree of small-scale variability, particularly in
176 the vertical (e.g., sharp vertical gradients of cloud microphysical processes and their
177 interactions with radiative forcing), which are typically poorly resolved by satellite and
178 conventional in situ observations. Furthermore, rapid error growth and systematic model
179 errors lead to large errors in the background forecast in precisely these regions, which are
180 poorly characterized by error covariance matrices based on climatology and/or sampling using
181 an ensemble of limited size. A field campaign has the potential to address some of these
182 difficulties by deploying specialized observing systems with high resolution and the ability to
183 measure both in and around clouds.

184 NAWDEX was proposed with the overarching hypothesis that diabatic processes have a
185 major influence on the jet stream structure, the downstream development of Rossby waves,
186 and eventually HIW. Specific science goals were formulated (Table 1), which require
187 observations of moisture advection in the boundary layer and of the vertical distribution of
188 stability, water vapor, liquid droplets and ice crystals. These observations will be used to
189 investigate spatial variability within clouds and the implications for diabatic processes.
190 Detailed wind measurements in the layer of the divergent outflow of the WCB are needed to
191 investigate the interaction of diabatically modified air masses with the upper-level jet. This
192 includes observations of horizontal and vertical gradients of wind, temperature and humidity
193 as well as hydrometeors in clouds. Accordingly, high-resolution cross-sections of wind,
194 temperature and humidity from the lower stratosphere down to the surface, inside and outside
195 of clouds, are the central observational requirement, which are not available from
196 conventional observations.

197 **EXPERIMENTAL DESIGN AND OBSERVATIONS.** The need for a new field
198 experiment emerged from a series of campaigns coordinated by the World Meteorological
199 Organization's program THORPEX (The Observing-System Research and Predictability
200 Experiment, Parsons et al. 2017). This series includes the Atlantic THORPEX Regional
201 Campaign (ATReC, Rabier et al. 2008), Winter Storm Reconnaissance (WSR, e.g., Szunyogh
202 et al. 2000), the THORPEX Pacific Asian Regional Campaign (T-PARC, Weissmann et al.
203 2011), and the Convective and Orographically induced Precipitation Study/European
204 THORPEX Regional Campaign (COPS/ETReC 2007, Wulfmeyer et al. 2011), which all
205 focused on the impact of additional observations on improving forecast accuracy. This idea
206 was pioneered by the Fronts and Atlantic Storm Track Experiment (FASTEX) in 1997 (Joly
207 et al. 1999) where the concept of targeting observations using sensitive area calculations was
208 introduced. The synthesis of these campaigns and data assimilation experiments denying
209 observations in data rich areas showed that the impact of targeted observations on global

210 forecast systems is weaker than originally anticipated, although they improve forecasts on
211 average (see review of Majumdar (2016)). At the same time, as discussed above, evidence
212 was growing that forecast errors often originate in regions where diabatic processes are
213 strong, and observation and modeling systems are least reliable. This provided the motivation
214 for a new campaign, NAWDEX, that rather than targeting regions of forecast sensitivity,
215 instead focused on observing the processes that are thought to be most uncertain in NWP
216 models.

217 Diabatic processes are difficult to measure directly, but can be constrained via their
218 observable effects on the structure and evolution of weather systems. In the decade before
219 THORPEX, detailed diagnostic case studies using aircraft measurements (e.g., ERICA
220 (Experiment on Rapidly Intensifying cyclones over the Atlantic, Hadlock and Kreitzberg
221 1988) and FASTEX) had already shown that diabatic processes, in particular diabatic heating
222 and cooling, can impact the large-scale dynamics via PV modification (Neiman et al. 1993;
223 Pomroy and Thorpe 2000). However, the processes are difficult to accurately quantify since
224 they depend on fine-scale structures (e.g., large gradients) in the water vapor and cloud fields
225 and are influenced by transport and mixing over a wide range of spatial and temporal scales
226 throughout the lifetime of the cyclone (recall Fig. 1). Two single-aircraft field campaigns
227 organized within THORPEX explored how aircraft observations could be used to accurately
228 constrain the impact of diabatic heating in midlatitude cyclones. DIAMET (DIAbatic
229 influence on Mesoscale structures in ExTropical storms; Vaughan et al. 2015) made
230 airborne in situ measurements of liquid droplets and ice crystals and used them to infer the
231 microphysical processes acting, their positions relative to mesoscale structures (such as fronts
232 and PV anomalies), and their role in the weather system dynamics. Although the observations
233 were limited to the 1-D aircraft flight path, they provided a basis for the modeling studies of
234 Dearden et al. (2014), who obtained estimates of heating rates from various microphysical
235 processes represented by a Lagrangian model initialized with in situ observations of size

236 distributions for cloud droplets and ice particles. However, using a model to extrapolate the
237 measurement information in space and time represents an additional source of uncertainty in
238 the quantification of the processes. The THORPEX-NAWDEX-Falcon project (Schäfler et al.
239 2014) attempted to constrain this uncertainty by carrying out in situ observations of clouds,
240 humidity and wind in ascending WCBs, and trying to re-sample the same air masses at a later
241 time to obtain a Lagrangian estimate of integrated diabatic effects. NAWDEX was conceived
242 to expand upon the design of these previous experiments by combining high resolution remote
243 sensing and in situ instrumentation to provide accurate measurements of atmospheric
244 structures including strong gradients, using multiple aircraft to sample air masses at different
245 stages of the WCB ascent and advection along the tropopause.

246 To allow these observations to be related to the development of weather forecast errors,
247 NAWDEX employed four research aircraft and ground-based stations spanning the northern
248 part of the North Atlantic with the aim of observing the processes influencing the
249 development of disturbances to the North Atlantic waveguide across the Atlantic. This
250 includes upstream triggering of disturbances on the waveguide by phenomena with strong
251 latent heat release, the continuous effects of clouds and radiation near the tropopause, the
252 dynamical interactions between large-scale disturbances, and the potential impact on weather
253 over Europe from the Mediterranean to Scandinavia.

254 *Airborne platforms and payload.* NAWDEX employed four research aircraft, the German
255 High Altitude and Long Range Research Aircraft (HALO) and the Deutsches Zentrum für
256 Luft- und Raumfahrt (DLR) Dassault Falcon 20, the French Service des Avions Français
257 Instrumentés pour la Recherche en Environnement (SAFIRE) Falcon 20, and the British
258 Facility for Airborne Atmospheric Measurements (FAAM) BAe 146. FAAM operated from
259 the UK and HALO and the two Falcon aircraft from Keflavik, Iceland, in an area covering the
260 North Atlantic, north of 45° N, and northern and central Europe. The payloads were chosen to

261 observe the required profiles of wind, temperature, moisture and cloud properties, and in the
262 case of FAAM, in situ cloud microphysics.

263 The strategy was to deploy HALO with its extended range to observe moisture transport
264 and diabatic processes in weather systems upstream of Iceland that impact the midlatitude
265 waveguide. HALO is a modified Gulfstream G-550 ultra-long-range business jet with a
266 maximum flight range of about 10000 km and a maximum endurance of 10 hours
267 (Krautstrunk and Giez 2012; Wendisch et al. 2016), which allows accessing remote regions
268 over the central North Atlantic that are not accessible by other European research aircraft. The
269 high ceiling of almost 15 km in combination with a sophisticated remote-sensing payload (see
270 sidebar and Table 2) allow HALO to fly above the main commercial aircraft routes and to
271 probe features of interest from above. The two Falcon aircraft, with a maximum range of 3000
272 km, a maximum endurance of about 4 hours and a ceiling up to 12 km, aimed to observe the
273 approaching cyclones and evolving jet streams close to Iceland. The DLR Falcon was
274 equipped with two wind lidar systems and the SAFIRE Falcon with a remote-sensing payload
275 for clouds and winds (sidebar and Table 2). The FAAM BAe 146, with a maximum endurance
276 of 5 hours and a ceiling of 10 km, was equipped with a range of in situ instrumentation for
277 meteorological, cloud and chemical measurements together with a downward-pointing aerosol
278 lidar and passive spectral radiometers. Its flights from East Midlands, UK, were aimed at
279 observing microphysics and turbulence in WCBs and the structure of the jet stream.

280 HALO, SAFIRE and the FAAM aircraft were equipped with dropsonde dispensers to
281 measure air temperature, wind and humidity profiles. Global NWP centers could access the
282 dropsonde data from HALO and SAFIRE via the Global Telecommunication System in near
283 real-time. The potential for coordinated application of the various instruments on board
284 multiple aircraft was realized through specific instrument-driven science goals (Table 1 and
285 sidebar). Table 2 indicates which of the research aims listed in Table 1 are addressed by each
286 instrument.

287 In parallel to NAWDEX, the NOAA (National Oceanic and Atmospheric Administration)
288 SHOUT (Sensing Hazards with Operational Unmanned Technology) campaign took place in
289 the tropical and subtropical western North Atlantic. SHOUT utilized the unmanned NASA
290 Global Hawk aircraft with a suite of remote-sensing platforms and dropsondes to study the
291 impact of the observations on TC forecasts. During the campaign, a tropical storm (TS)
292 moved into the midlatitudes and underwent ET, providing an unprecedented scientific
293 opportunity to observe the interaction of such a system with the jet stream using a
294 combination of upstream flights with the SHOUT Global Hawk and downstream flights with
295 NAWDEX aircraft.

296 **[Place Sidebar 1 here: Active remote-sensing observations for future satellite missions**
297 **Aeolus and EarthCARE]**

298 *Airborne observations.* NAWDEX observations took place in the North Atlantic basin
299 between 17 Sep and 22 Oct 2016. Figure 2 shows the tracks of the 47 research flights of the
300 four aircraft, together amounting to 205 flight hours. Performing research flights over the
301 North Atlantic is complicated because of the dense trans-Atlantic air traffic. Commercial
302 airliners are tightly staggered along predefined flight routes, the so-called North Atlantic
303 Tracks (NATs), between altitudes of 9 and 12 km. Operating research aircraft beneath the
304 NATs offers high flexibility for the flight planning; however, the base height of the NATs is
305 often too low to observe the tropopause and jet-related maximum wind speeds. Furthermore
306 the location of the NATs changes from day to day, depending on the forecast wind situation.
307 Height changes and the release of dropsondes from high altitudes are not possible in the NAT
308 area. The requirement of air traffic control (ATC) authorities to have detailed flight plans 2-3
309 days in advance created challenging circumstances in weather situations with reduced
310 predictability, i.e., in situations with large changes between subsequent forecasts. Therefore,
311 NAWDEX combined modern forecasting tools including ensemble and adjoint-based

312 diagnostics, and new visualization techniques to incorporate forecast uncertainty in the
313 planning process (see sidebar on forecast products).

314 HALO covered large parts of the central and eastern North Atlantic and reached flight
315 distances up to 7150 km (~9 h). The flights were performed either at altitudes between 11.5
316 and 14.2 km above the NATs for remote-sensing observations or at ~8 km to release
317 dropsondes beneath the NATs. The two Falcon aircraft remained in radar-controlled air
318 spaces near Greenland, Iceland and the UK. The FAAM BAe 146 flights were north and west
319 of the UK. A total of 289 dropsondes were released (Fig. 3a).

320 **[Sidebar 2: Forecast products to investigate forecast uncertainty]**

321 The research flights occurred within 13 Intensive Observation Periods (IOPs), which were
322 consecutively numbered and had a duration of 1-6 days. Each IOP was associated with a
323 particular weather system development and addressed one or more NAWDEX science
324 objectives (Table 3). For easier communication, the IOPs were given names, which either
325 correspond to the cyclone naming of the Free University of Berlin or the National Hurricane
326 Center, or were invented by the NAWDEX team (Table 3). Some IOPs overlap in time when
327 different weather systems were observed simultaneously by the different aircraft.

328 To exploit instrument synergies and enable direct instrument comparisons, coordinated
329 flights were performed, i.e., the same air mass was near-simultaneously probed by different
330 aircraft on common flight legs. In total, 16 coordinated legs, with a total flight time of 14.5 h
331 and a distance of about 10000 km, were achieved. The longest coordinated leg with the
332 SAFIRE Falcon and HALO on 14 Oct 2016 had a distance of 1365 km (1.8 h). On two
333 occasions the coordination involved three aircraft: HALO and the two Falcons flew together
334 for ~30 min (~300 km) on 9 Oct between the UK and Iceland, and on 14 Oct, FAAM, HALO
335 and the SAFIRE Falcon had a common leg between the Faroe Islands and Scotland (55 min,
336 570 km).

337 ***Ground-based facilities and observations.*** During several IOPs additional ground-based
338 observations were taken to complement the aircraft operations and to enhance the temporal
339 and spatial coverage of routine observations. In total 589 additional radiosondes from 40
340 stations in 14 countries were launched (Fig. 3b and Table 4). Of these launches, 253 were
341 achieved through the cooperation of national meteorological agencies in the European
342 Meteorological Services Network (EUMETNET), complemented by additional radiosondes
343 from Iceland, UK, France and Norway. Launches from land stations or commercial ships
344 were requested daily depending on the predicted evolution of weather systems. Furthermore,
345 two additional radiosondes were launched daily during the campaign from six stations in
346 eastern Canada, upstream of the main NAWDEX area (336 in total).

347 Special ground-based observations were conducted in Iceland, the UK and France (Fig.
348 3b). At Keflavik airport, a radiosonde facility was set up by DLR to increase the frequency of
349 the operational soundings. In cases of orographically induced gravity waves (GWs), large
350 balloons were launched to reach altitudes up to 42 km. Also in Keflavik, a Doppler cloud
351 radar BASTA (Delanoë et al. 2016) allowed several comparisons with its airborne counterpart
352 on board the SAFIRE Falcon during overflights. In the UK, a mesosphere–stratosphere–
353 troposphere (MST) radar, Raman lidar, and radiosondes were operated at Capel Dewi
354 (Wales), together with another MST radar wind profiler at South Uist (Scotland).
355 Additionally, the MST radar at Andøya, Norway, measured tropospheric winds upon request.
356 Two observational sites were active in France during the campaign. The site in Lannion
357 (Brittany) operated a wind profiler, the BASTA Doppler cloud radar and a GPS station. The
358 Site Instrumental de Recherche par Télédétection Atmosphérique (SIRTA) near Paris
359 (Haeffelin et al. 2005) operated radar and lidars, and launched radiosondes.

360 **METEOROLOGICAL CONDITIONS.** The fall of 2016 was a favorable period for
361 observing midlatitude weather over the North Atlantic. The average synoptic situation for the

362 campaign period was characterized by an increased frequency of relevant weather systems
363 compared to climatology (Fig. 4). One of the most prominent features was a long-lasting
364 blocking high and surface anticyclone covering large parts of Scandinavia (Fig. 4a).
365 Extratropical cyclones occurred more frequently than normal south of Iceland and Greenland
366 (Fig. 4b), in the core area of airborne NAWDEX observations. Consistent with the increased
367 frequency of cyclones relative to climatology, the WCB frequency (Fig. 4c) shows increased
368 activity over large parts of the North Atlantic. During the campaign, a succession of events
369 with poleward transport of warm air and ascent of low-PV air into the upper troposphere was
370 observed that appeared to strengthen the downstream anticyclonic anomaly. Most midlatitude
371 cyclones (Fig. 4d) approached Iceland from the southwest, which was favorable for reaching
372 them with Falcon flights from Keflavik. Only a small fraction of the extratropical cyclones
373 moved into central and northern Europe. Six TS occurred during NAWDEX. Ian (12-16 Sep),
374 Julia (13-16 Sep), Karl (14-25 Sep) and Lisa (19-25 Sep) did not exceed TS strength, while
375 Matthew (29 Sep-9 Oct) and Nicole (4-18 Oct) were classified as major hurricanes. Ian, Karl
376 and Nicole underwent ET and moved far into the midlatitudes. TPVs originating over the
377 Canadian polar region were observed twice when they moved southward over the Davis Strait
378 and interacted with the midlatitude waveguide.

379 North Atlantic weather regimes during NAWDEX show Scandinavian blocking to be the
380 dominant regime (blue line in Fig. 5a), corresponding to the anomalous anticyclone activity
381 over northern Scandinavia (Fig. 4a). In late September the block decayed and a short period
382 with a positive North Atlantic Oscillation (NAO) prevailed before the Scandinavian blocking
383 pattern was again established.

384 A broad measure of forecast quality during NAWDEX is provided by the anomaly
385 correlation coefficient (ACC) of the mid-tropospheric geopotential height pattern over the
386 eastern North Atlantic as predicted by the ECMWF Integrated Forecasting System (IFS) in
387 fall 2016 (Fig. 5b). Periods of increased 120-h forecast errors and high spread in the ensemble

388 forecasts are evident, and four of these periods were directly relevant to NAWDEX. Three
389 periods of reduced forecast skill (23 to 27 Sep, 29 Sep to 3 Oct and 5 to 10 Oct) occurred
390 during NAWDEX and two periods of the four were accompanied by a weather regime
391 transition (Fig. 5a). Forecast uncertainty was high on 26 Sep during the onset of a positive
392 NAO phase, and on 1 Oct during the return to the Scandinavian blocking regime. High
393 uncertainty also occurred prior to the campaign, for forecasts initialized between 10 and 14
394 Sep, again covering a regime transition to Scandinavian blocking. This period affected
395 NAWDEX as it complicated the planning of the transfer flight to Keflavik (IOP 1) five days
396 later.

397 The progression of weather systems across the North Atlantic during NAWDEX can be
398 conveniently described as a storyline characterized by *upstream triggers*, their dynamic
399 *interaction* with the jet stream, *subsequent development* of disturbances, and downstream
400 *weather impacts* over Europe. Three such sequences occurred completely within the
401 NAWDEX period, and their timespan is indicated by dark grey shading in Fig. 5. In each
402 case, low predictability was found in 5-day forecasts for the eastern North Atlantic initialized
403 within the *trigger* stage (marked by a drop in forecast skill in Fig. 5b), while the final *impact*
404 stage was associated with significant changes in the weather over Europe at the verification
405 time 5 days later. The snapshots for each sequence in Fig. 6 show that the interaction of the
406 trigger disturbance with the waveguide featured intensification of a surface cyclone, with a
407 diabatic contribution consistent with the first three regions identified in the conceptual model
408 presented in Fig. 1. However, the subsequent development and impact stages differed
409 markedly, with the pattern of low PV in the downstream ridge affecting weather even further
410 downstream than suggested by region 4 of Fig. 1. The temporal continuity between the
411 snapshots in Fig. 6 is shown by labeling several coherent long-lived features (identified in the
412 caption). Prominent ridges (R1-R9) along the North Atlantic waveguide are identified as

413 northward excursions of the jet stream (and the PV gradient). Since each ridge is
414 characterized by low PV air, the associated flow tends to be anticyclonic.

415 Sequence A is *triggered* by TS Karl leaving the subtropics and moving northwards into
416 the midlatitudes (Fig. 6, panel A.1). Large ensemble spread and changes between consecutive
417 forecast runs showed that the subsequent evolution was very sensitive to uncertainties in the
418 location and timing of the interaction of Karl with ridge R2, the trough upstream, and the
419 associated weak surface cyclone (not shown). The *interaction* that took place was a merging
420 of Karl with a low-level cyclone, leading to rapid re-intensification and the formation of a
421 cyclonic hook at tropopause level separating ridge R2 from the new ridge R3 (Fig. 6 A.2).
422 The ridge-building is intensified by diabatically produced low PV in the WCB outflow. Hence
423 in the subsequent *development*, the jet stream is unusually strong on its southern flank,
424 forming a jet streak that propagates ahead from Karl reaching Scotland the following day
425 (Fig. 6 A.3). The *impact* on European weather occurs through the formation of a new cyclone
426 Walpurga (W in Fig. 6 A.4), which develops to the west of ridge R3 helping to amplify it.
427 Moisture laden air on the western flank of ridge R3 is drawn around the subtropical high.
428 During IOP 5, HALO observed the moist boundary layer in this atmospheric river type flow
429 that extends to Norway where it causes heavy, persistent rainfall, similar to the case studied in
430 Sodemann and Stohl (2013).

431 Sequence B begins as sequence A ends, in a southwesterly flow situation with a long PV
432 streamer that formed through the merger of the trough west of R3 and the large cut-off feature
433 C (Fig. 6 A.3-A.4). The *trigger* for this sequence appears to follow from the vortex roll-up of
434 the streamer through shear instability, resulting in a new cut-off over Newfoundland (V in
435 Fig. B.1), which then *interacts* and merges with a large-scale trough west of R5 advancing
436 rapidly from the northwest. Note that ridge R5 and its upstream trough wrap up cyclonically
437 during the development so that the trough catches up with the cut-off to the south of R5. The
438 tropopause was very low just in the very center of this system, which therefore has been

439 named the “stalactite cyclone” (St in Fig. 6 B.2). In the *development* stage, a second cyclone
440 (F in Fig. 6 B.3) intensified rapidly between ridge R6 and the trough to its west. The poleward
441 moving air in R6 crossed Iceland and reinforced the anticyclonic anomaly formed by ridge R5
442 of the stalactite cyclone. The *impact* of the sequence comes not as a classical severe weather
443 event, but through the establishment of a strong blocking anticyclone over Northern Europe,
444 which persisted for the next two weeks.

445 Sequence C begins with two upstream *triggers*. A TPV originating in the Canadian Arctic
446 is carried rapidly southeastward on the poleward flank of the jet stream (T in Fig. 6 B.4 and
447 C.1). It is hypothesized that the TPV locally enhanced the cyclonic circulation about the tip of
448 the large-scale trough (T in Fig. 6 C.1), which eventually wrapped cyclonically over Iceland
449 (Fig. 6 C.2). At the same time the remnants of cut-off C appear to be associated with the
450 emergence of a small surface cyclone, which has been named “Sanchez” (S in Fig. 6 C.1).
451 The European dipole block (cf. Rex et al. 1950) is well established at this time so that the
452 ridge R8 and the cyclonic PV anomaly over Iceland are held stationary and a PV filament
453 forms in the deformation region on their western side. The filament is unstable and
454 experiences vortex roll-up, forming three tropopause-level cyclonic vortices. The key
455 *interaction* in this sequence occurs as the low-level cyclone Sanchez passes the southernmost
456 cut-off, but then phase-locks with the central cut-off resulting in baroclinic intensification (S
457 in Fig. 6 C.2). As the sequence *develops*, the resulting cut-off cyclone progresses slowly
458 eastwards (Fig. 6 C.3) and is responsible for some of the most dramatic high *impact* weather
459 during NAWDEX, with heavy precipitation and flooding across southern France and
460 northwestern Italy in the southerly flow ahead of it (Fig. 6 C.4). But this HIW is not the only
461 significant outcome of Sequence C. Returning to stage C.2, ridges R8 and R9 are similar in
462 horizontal extent, but the tropopause is much higher above R9 than R8 (not shown) with the
463 result that the anticyclonic circulation induced by R9 is stronger and R8 is stretched out
464 meridionally between R6 and R9 (Fig. 6 C.3). As NAWDEX draws to a close, the ridge R9

465 extends rapidly into the Arctic, reinforcing the block and forming a PV anomaly in the shape
466 of the Icelandic character Þ (the first letter of Þor - pronounced Thor - the ancient Norse god
467 of HIW).

468 It is important to note that the large-amplitude ridge building leading to the Thor block is
469 not R8, which developed as part of the interaction phase of Sequence C, but rather R9,
470 associated with a second cyclone that develops to the west (and which may play a role in the
471 cut-off of Sanchez). Indeed for all three sequences, the development stage leading to weather
472 impacts over Europe appears to be associated with a second cyclone that forms in an
473 environment modified by the interaction of the trigger disturbance with the midlatitude flow,
474 and whose development is difficult to predict because of the low predictability of the
475 environment.

476 **HIGHLIGHTS OF NAWDEX.** Observations in NAWDEX were organized in IOPs that
477 focused on key weather systems involved in the longer sequences (Table 5). Several of these
478 IOPs are unprecedented in terms of the phenomena that were sampled or the comprehensive
479 coverage and multi-faceted nature of the measurements. While the analysis of the data is just
480 beginning, a first impression of the results can be obtained from four highlights that illustrate
481 the unique sets of multi-platform and multi-instrument observations that were obtained.

482 *Extratropical transition of TS Karl.* The evolution of TS Karl is the central feature of
483 Sequence A discussed above and IOP 4. It was the first extratropical transition sequence that
484 has been observed with research aircraft through at all stages of development, including TS
485 status, ET, re-intensification with impacts on jet stream strength, moisture transport and
486 downstream HIW (Table 5). By flying over the TS and its northwestern flank twice, the
487 SHOUT Global Hawk observed the development stage that occurred far south of the
488 midlatitude jet stream on 22/23 Sep (Fig. 7a), and the ET phase on 24/25 Sep (Fig. 7b). On 26
489 Sep, HALO observed the interaction with the waveguide and re-intensification phase of the

490 storm by flying over the cyclone center (Fig. 7c), WCB ascent, the low-valued PV air in the
491 WCB outflow and the dry intrusion (not shown). When Karl moved rapidly towards Scotland,
492 decaying in strong horizontal shear on 27 Sep, IOP 5 focused on the intense jet streak at
493 tropopause level and the strong moisture transport along the equatorward side of the jet with a
494 combination of HALO, FAAM and DLR Falcon flights (Fig. 7d).

495 IOP 4 will contribute to answer several of the posed research questions (see Table 1 and
496 3). The large number of dropsonde and special radiosonde measurements that were
497 assimilated into operational forecasts in real-time will provide a basis for observational
498 impact and predictability studies. Detailed airborne remote-sensing observations will allow
499 examination of the role of diabatic processes and their representation in numerical models.
500 Both the synergies of the instruments and the storm-following observational strategy give
501 unprecedented information about this intense and long-lived cyclone and a unique opportunity
502 to analyze forecast error growth due to in situ processes vs. downstream propagation.

503 ***Cloud physics in a WCB.*** IOP 3 focused on observing the vertical cloud structure and cloud
504 microphysical processes in a WCB that was related to the midlatitude cyclone Vladiana south
505 of Iceland and west of Scotland on 23 Sep 2016 (Fig. 7a and Table 5). The WCB transported
506 moist air northeastward just west of the UK as indicated by the low-valued PV air in the upper
507 troposphere (Fig. 8a).

508 HALO first stayed beneath the NATs at altitudes of ~8 km on the way to the
509 southwestern-most point of the flight (white circle) to begin the first of three sections across
510 the WCB. On this leg to Ireland, 12 dropsondes were released before HALO climbed to ~13
511 km in Irish airspace. Over northern Ireland, HALO and FAAM joined to perform coordinated
512 remote-sensing and in situ observations of the WCB. HALO measured the WCB by remote-
513 sensing from above while FAAM performed 4 in situ legs at different altitudes to measure

514 cloud-microphysical parameters inside the WCB. After the coordinated leg, HALO crossed
515 the WCB a third time and observed the outflow of the WCB between Scotland and Iceland.

516 Figure 8 focuses on the first and second crossing of the WCB. The WALES lidar
517 measured water vapor profiles throughout the troposphere and lower stratosphere in the
518 absence of clouds (Fig. 8b). At the western side of the cross-sections, where HALO was
519 located on the stratospheric side of the waveguide, the post-frontal troposphere was cloud-free
520 except for boundary layer clouds reaching up to 2 km. The water vapor shows high
521 variability, which portrays the dynamically modulated transport of moisture related to cyclone
522 Vladiana. On both crossings of the waveguide, one west-to-east and one east-to-west, a tilted
523 dry layer is visible at altitudes between 5 and 9 km (1110-1125 and 1305-1325 UTC), related
524 to a dry intrusion west of the low-level cold front. The wedge-shaped moist layer on top is
525 associated with high moisture values in the WCB outflow. The second crossing at high
526 altitudes depicts a strong vertical moisture gradient, on top of the elevated moist layer, that
527 marks the tropopause and extends further east into the area where WCB clouds reach high
528 altitudes. A decrease of the tropopause height is detected towards the west on the second leg.
529 The radar shows two vertically (~11.5 km) and horizontally (~400 km) extended and coherent
530 clouds (Fig. 8c) representing the double crossing of the WCB. In between, i.e., on the eastern
531 side of the WCB, cloud tops are lower and the clouds are intermittent. The sharp vertical
532 gradient in radar reflectivity at about 3 km altitude marks the melting layer.

533 On the second transect the FAAM aircraft performed in situ measurements on flight legs
534 beneath HALO (Figs. 8b,c). HALO met FAAM at the beginning of its second WCB leg
535 (purple diamond marker in Fig. 8c) where FAAM started its lowest leg at about 3 km altitude,
536 just above the melting layer, with subsequent legs at 4, 6 and 7.5 km. The in situ observations
537 show that both mixed-phase and ice-only clouds were encountered during the low-level run,
538 but during the high-level runs only ice was observed. The ice water content (IWC) in the
539 WCB shows maximum values of 0.4 g m^{-3} on the lowest two legs (Fig. 8d). Ice images show

540 large differences in the form of the particles at different altitudes. On the lowest leg, large
541 aggregates (~6 mm) dominate close to the freezing level, while on the highest level higher
542 concentrations of small irregularly shaped crystals (< 1 mm) prevail.

543 HALO also observed the interaction of Vladiana's WCB outflow with the jet stream in
544 coordination with the DLR Falcon (not shown). IOP 3 contributes to all research aims (Table
545 3) and future work on the cloud microphysics observations will investigate, e.g., the
546 correlation of increased IWC with particularly high radar reflectivity. Data from liquid and ice
547 particle size distributions will be used to improve the retrieval of cloud properties from the
548 HALO remote-sensing instruments. Overall, this is a unique set of comprehensive and
549 complementary airborne observations of a WCB, its embedded microphysical processes and
550 its outflow interaction with the jet stream.

551 ***Wind observations in the jet stream and outflow of a WCB.*** Figure 6 (panel B.2) shows the
552 stalactite cyclone that formed previously via merging of two near-surface vorticity maxima
553 with a very intense, small-scale, upper-level PV anomaly south of Newfoundland (not
554 shown). The rapid development of the cyclone occurred in the mid-Atlantic between 30 Sep
555 and 2 Oct. On 2 Oct (IOP 6), a coordinated flight of the DLR and SAFIRE Falcons observed
556 WCB ascent and outflow when the stalactite cyclone was most intense (Fig. 9a). The aircraft
557 flew together to intersect the jet stream on the northwestern edge of ridge R5 wrapping
558 cyclonically around the stalactite cyclone. On a common leg between Iceland and Greenland
559 both aircraft crossed the jet stream (Fig. 9b) and made complementary wind observations
560 (Figs. 9c,d). The DWL lidar on the DLR Falcon observed two wind maxima up to 50 m s^{-1} in
561 cloud-free regions and in optically thin cirrus in the WCB outflow. Complementarily, the
562 SAFIRE radar observed in-cloud winds in the region of WCB ascent in the mid and lower
563 troposphere. Only in dry and aerosol-poor air masses over Greenland, i.e., on the stratospheric
564 side of the waveguide, the combination of both instruments provides poor data coverage. The

565 SAFIRE Falcon released 9 dropsondes when crossing the jet stream, yielding further profiles
566 of winds, temperature and moisture.

567 Future research on IOP 6 will be mainly dedicated to predictability issues associated with
568 the blocking formation downstream of the cyclone. The block formed at the time when a loss
569 of predictability in the ECMWF forecasts occurred (Fig. 5b). Winds measured by the two
570 aircraft will help to characterize the role of the WCB outflow in the ridge building. The
571 observed high winds and strong vertical gradients were repeatedly observed on flights across
572 the jet stream with observed maxima up to 80 m s^{-1} and often related to strong vertical wind
573 speed gradients up to $30 \text{ m s}^{-1} \text{ km}^{-1}$. A unique aspect of this example is the benefit of
574 coordinated flights with complementary instruments to address one the key objectives of
575 NAWDEX (Table 1 and 3) – observing the strong wind shear and PV gradients near a WCB
576 outflow.

577 *HIW related to cut-off cyclone Sanchez.* Cut-off Sanchez was initiated in the central North
578 Atlantic and reached southern Europe between 12 and 14 Oct 2016 (Fig. 6, Seq. C). On its
579 leading edge moisture was advected northward (Fig. 10a) on 13 Oct when it triggered heavy
580 precipitation and strong winds over France and Italy. The 24-hour accumulated precipitation
581 in the Hérault region reached $\sim 250 \text{ mm}$ (Figs. 10b), and wind gusts exceeding 100 km h^{-1}
582 were observed along the French Mediterranean coast (Figs. 10c). As in typical Cevenol
583 episodes, strong southerlies brought warm and moist air from the Mediterranean Sea toward
584 the Massif Central and caused heavy orographic precipitation over the mountain ranges of the
585 Cévennes. Upper-level cut-offs like Sanchez are known to be favorable synoptic conditions
586 for triggering convective mesoscale events (Nuissier et al. 2008), which were intensively
587 studied during the recent international field campaign HyMex (Ducrocq et al. 2016). Part of
588 the air masses responsible for the HIW subsequently reached as far north as the SIRTA site
589 near Paris, causing precipitation in the afternoon of 13 Oct (Fig. 10d). This episode illustrates

590 one of the key NAWDEX aims (Table 1) to investigate how HIW events over Europe are
591 associated with complex waveguide dynamics (in this case the formation of a PV cut-off)
592 over the upstream North Atlantic. The combination of the ground-based data with NAWDEX
593 observations both from aircraft and from the many additional radiosondes taken during IOP 9
594 will enable detailed studies of the forecast sensitivity of HIW to upstream initial condition
595 errors.

596 **SUMMARY.** NAWDEX was the first field experiment with synergistic airborne and ground-
597 based observations from the entrance to the exit region of the climatological storm track,
598 taken to investigate the role of diabatic processes in altering jet stream disturbances, their
599 development, and effects on HIW downstream.

600 Because of the operational limitations on research aircraft flights over the North Atlantic
601 and Europe and the need for high-resolution profile measurements of thermal and dynamic
602 properties, NAWDEX focused on airborne remote-sensing observations and the deployment
603 of multiple aircraft. Advanced instruments for remote sensing of wind, water vapor and cloud
604 properties provide an integrated picture of the atmospheric structure in regions where diabatic
605 processes were active, from the synoptic to sub-kilometer scale. The unique combination of
606 the four aircraft and the first deployment of HALO in a campaign focusing on midlatitude
607 dynamics allowed observations in large parts of the North Atlantic. Often, the same weather
608 system could be sampled at different stages of its development, and the interaction of
609 successive weather systems have been observed following the NAWDEX storyline.
610 Additional ground-based observations and an enhanced density of operational radiosonde
611 releases yielded very high coverage with high-resolution vertical profiles from the ground to
612 the lower stratosphere. The region with enhanced atmospheric profiling extended from eastern
613 Canada to most parts of Europe. The coverage and fidelity of the resulting observations will
614 enable future studies to estimate diabatic heating through the use of models and diagnostics

615 constrained by the NAWDEX observations, particularly in situations when the atmospheric
616 flow is especially sensitive to small changes in diabatic heating. Over the 13 IOPs it was
617 possible to address all original campaign objectives (Table 1 and 3). Table 5 lists a number of
618 particular highlights and “firsts” that have drawn the attention of the NAWDEX scientists.

619 The success of the observational campaign was possible because of the favorable
620 meteorological conditions, with many cyclones and WCBs in the vicinity of Iceland.
621 Importantly, the NAWDEX period contained episodes of reduced predictability, indicating
622 that uncertainties originating in the estimated atmospheric state and model formulation grew
623 rapidly. The suggestion that these uncertainties spread via their impact on the lifecycle of a
624 “second cyclone” forming to the west, rather than through a process of downstream
625 development, shows that NAWDEX has the potential to make an important contribution to
626 the study of predictability of midlatitude weather and the representation of uncertainty in
627 EPSs. Since there were also episodes of HIW in Europe connected to disturbances of the
628 North Atlantic waveguide, NAWDEX also is a unique opportunity to explore HIW
629 predictability.

630 To the best of our knowledge, the NAWDEX period provides the most complete set of
631 combined wind, humidity, temperature and cloud profile observations of the North Atlantic
632 jet stream yet accomplished. This dataset will form the basis of detailed case studies and the
633 evaluation of weather and climate prediction models for many years. The widespread
634 coverage of high-resolution multi-variate cross-sections across the jet stream and weather
635 systems developing from one side of the North Atlantic to the other enables examination of
636 the whole chain of processes from the triggering of disturbances on the waveguide to the
637 ultimate impact on weather systems affecting Europe.

638

639 **ACKNOWLEDGMENTS.** Many international institutions contributed to the implementation
640 of NAWDEX and the results presented in this overview article. NAWDEX was only possibly
641 due to the close cooperation of many colleagues including the planning team, the instrument
642 groups and the flight operations (Appendix A). The HALO and DLR Falcon campaign
643 received funding from DLR (project “Klimarelevanz von atmosphärischen Spurengasen,
644 Aerosolen und Wolken” KliSAW), ETH Zurich, NRL Monterrey, the German Science
645 Foundation (DFG; within SPP1294 HALO and SFB/TRR165 Waves to Weather), the
646 European Facility for Airborne Research (EUFAR, project NAWDEX Influence) and the
647 European Space Agency (ESA, providing funds related to the preparation of Aeolus
648 (WindVal II, contract No. 4000114053/15/NL/FF/gp) and EarthCARE (EPATAN, contract
649 No. 4000119015/16/NL/CT/gp)). Special thanks are due to the Max Planck Institute Hamburg
650 for sharing the HALO payload during the NARVAL-II and NAWDEX campaigns in summer
651 and fall 2016 and for their general support of NAWDEX. We are grateful to the DLR flight
652 experiments team; in particular the colleagues of flight operations for the careful preparation
653 and the outstanding support in Keflavik. The authors are grateful to the HALO and Falcon
654 pilots and the technical and sensor team from DLR flight operations for excellent support
655 prior and during NAWDEX. The SAFIRE Falcon contribution to NAWDEX received direct
656 funding from IPSL, Météo-France, INSU-LEFE, EUFAR-NEAREX and ESA (EPATAN,
657 contract No. 4000119015/16/NL/CT/gp). The UK funding for the FAAM aircraft flights,
658 dropsondes and additional radiosondes was provided by the Met Office. Special thanks are
659 due to the SHOUT mission for their open collaboration which enabled coordinated
660 observations of tropical storm Karl. Observations at Capel Dewi were funded by the National
661 Centre for Atmospheric Science. We thank the European Meteorological Service Network
662 (EUMETNET) for funding additional radiosondes and for providing access to the data.
663 Environment and Climate Change Canada provided funding for enhanced radiosonde
664 frequency during the campaign. The Icelandic Meteorological Office and DLR are thanked

665 for providing additional radiosondes from Iceland. We thank ECMWF for providing access to
666 data in the framework of the Support Tool for HALO Missions (SPDEHALO) special project.
667 We gratefully acknowledge many discussions with US colleagues, in particular Chris Davis,
668 Pat Harr and Heather Archambault, during the scientific preparation of NAWDEX. We thank
669 Michael Sprenger (ETH Zurich) for preparing the data for Fig. 4. MB and CMG acknowledge
670 funding from the Swiss National Science Foundation (Projects 200020_165941 and
671 PZ00P2_148177, respectively). JDD and CAR acknowledge the support of the U.S. Navy
672 Chief of Naval Research through the NRL Base Program PE 0601153N, and the ONR PE
673 0602435N.

674 **APPENDIX A: The NAWDEX Team**

675 Table A1

676 **REFERENCES**

- 677 Agusti-Panareda, A., C. D. Thorncroft, G. C. Craig, and S. L. Gray, 2004: The extratropical
678 transition of hurricane Irene (1999): A potential-vorticity perspective. *Quart. J. Roy.*
679 *Meteor. Soc.*, **130**, 1047–1074.
- 680 Archambault, H. M., L. F. Bosart, D. Keyser, and J. M. Cordeira, 2013: A climatological
681 analysis of the extratropical flow response to recurving western North Pacific tropical
682 cyclones. *Mon. Wea. Rev.*, **141**, 2325–2346.
- 683 Bauer, P., A. Thorpe, and G. Brunet, 2015: The quiet revolution of numerical weather
684 prediction. *Nature*, **525**, 47–55.
- 685 Binder, H., M. Boettcher, H. Joos, and H. Wernli, 2016: The role of warm conveyor belts for
686 the intensification of extratropical cyclones in Northern Hemisphere winter. *J. Atmos. Sci.*,
687 **73**, 3997–4020.
- 688 Brogniez, G., C. Pietras, M. Legrand, P. Dubuisson, and M. Haeffelin, 2003: A high-accuracy
689 multiwavelength radiometer for in situ measurements in the thermal infrared. Part II:
690 Behavior in field experiments. *J. Atmos. Oceanic Technol.*, **20**, 1023–1033.
- 691 Browning, K. A., M. E. Hardman, T. W. Harrold, C. W. Pardoe, 1973: Structure of rainbands
692 within a mid-latitude depression. *Quart. J. Roy. Meteor. Soc.*, **99**, 215–231.
- 693 Bruneau, D., J. Pelon, F. Blouzon, J. Spatazza, P. Genau, G. Buchholtz, N. Amarouche, A.
694 Abchiche, and O. Aouji, 2015: 355nm high spectral resolution airborne lidar LNG: system
695 description and first results. *Appl. Opt.*, **54**, 8776–8785.
- 696 Carlson, T. N., 1980: Airflow through midlatitude cyclones and the comma cloud pattern.
697 *Mon. Wea. Rev.*, **108**, 1498–1509.
- 698 Cavallo, S. M., and G. J. Hakim, 2010: Composite structure of tropopause polar cyclones.
699 *Mon. Wea. Rev.*, **138**, 3840–3857.

700 Chaboureau, J.-P., and C. Claud, 2006: Satellite-based climatology of Mediterranean cloud
701 systems and their association with large-scale circulation. *J. Geophys. Res.*, **111**, D01102,
702 doi: 10.1029/2005JD006460.

703 Chagnon, J., S. L. Gray, and J. Methven, 2013: Diabatic processes modifying potential
704 vorticity in a North Atlantic cyclone. *Quart. J. Roy. Meteor. Soc.*, **139**, 1270–1282.

705 Davis, C. A., M. T. Stoelinga, and Y.-H. Kuo, 1993: The integrated effect of condensation in
706 numerical simulations of extratropical cyclogenesis. *Mon. Wea. Rev.*, **121**, 2309–2330.

707 Delanoë, J., A. Protat, O. Jourdan, J. Pelon, M. Papazzoni, R. Dupuy, J.-F. Gayet, and C.
708 Jouan, 2013: Comparison of airborne in-situ, airborne radar-lidar, and spaceborne radar-
709 lidar retrievals of polar ice cloud properties sampled during the POLARCAT campaign. *J.*
710 *Atmos. Oceanic Technol.*, **30**, 57–73.

711 Delanoë, J., A. Protat, J.-P. Vinson, W. Brett, C. Caudoux, F. Bertrand, J. Parent du Chatelet,
712 R. Hallali, L. Barthes, M. Haeffelin, and J.-C. Dupont, 2016: BASTA: A 95-GHz FMCW
713 Doppler Radar for Cloud and Fog Studies. *J. Atmos. Oceanic Technol.*, **33**, 1023–1038.

714 Doyle, J. D., C. Amerault, C. A. Reynolds, and P. A. Reinecke, 2014: Initial condition
715 sensitivity and predictability of a severe extratropical cyclone using a moist adjoint. *Mon.*
716 *Wea. Rev.*, **142**, 320–342.

717 Ducrocq, V., S. Davolio, R. Ferretti, C. Flamant, V. H. Santaner, N. Kalthoff, E. Richard, and
718 H. Wernli, 2016: Introduction to the HyMeX Special Issue on ‘Advances in understanding
719 and forecasting of heavy precipitation in the Mediterranean through the HyMeX SOP1
720 field campaign’. *Quart. J. Roy. Meteor. Soc.*, **142**, 1–6.

721 Ehrlich, A., E. Bierwirth, M. Wendisch, J.-F. Gayet, G. Mioche, A. Lampert, and J.
722 Heintzenberg, 2008: Cloud phase identification of Arctic boundary-layer clouds from
723 airborne spectral reflection measurements: test of three approaches. *Atmos. Chem. Phys.*, **8**,
724 7493–7505

725 ESA European Space Agency, 2008: ADM-Aeolus Science Report, ESA SP-1311, ISBN 978-
726 92-9221-404-3, 121 pp.

727 Ewald, F., T. Kölling, A. Baumgartner, T. Zinner, and B. Mayer, 2015: Design and
728 characterization of specMACS, a multipurpose hyperspectral cloud and sky imager. *Atmos.*
729 *Meas. Tech.*, **9**, 2015–2042.

730 Frame, T. H. A., J. Methven, N. M. Roberts, and H. A. Titley, 2015: Predictability of frontal
731 waves and cyclones. *Wea. Forecasting*, **30**, 1291-1302.

732 Grams, C. M., H. Wernli, M. Boettcher, J. Campa, U. Corsmeier, S. C. Jones, J. H. Keller, C.
733 J. Lenz, and L. Wiegand, 2011: The key role of diabatic processes in modifying the upper
734 tropospheric wave guide: a North Atlantic case-study. *Quart. J. Roy. Meteor. Soc.*, **137**,
735 2174–2193.

736 Grams, C. M., and S. R. Blumer, 2015: European high-impact weather caused by the
737 downstream response to the extratropical transition of North Atlantic Hurricane Katia
738 (2011). *Geophys. Res. Lett.*, **42**, 8738–8748.

739 Grams, C. M., and H. M. Archambault, 2016: The key role of diabatic outflow in amplifying
740 the midlatitude flow: a representative case study of weather systems surrounding western
741 North Pacific extratropical transition. *Mon. Wea. Rev.*, **144**, 3847–3869.

742 Gray, S. L., C. Dunning, J. Methven, G. Masato, and J. Chagnon, 2014: Systematic model
743 forecast error in Rossby wave structure. *Geophys. Res. Lett.*, **41**, 2979–2987.

744 Haeffelin, M., L. Barthès, O. Bock, C. Boitel, S. Bony, D. Bouniol, H. Chepfer, M. Chiriaco,
745 J. Cuesta, J. Delanoë, P. Drobinski, J.-L. Dufresne, C. Flamant, M. Grall, A. Hodzic, F.
746 Hourdin, F. Lapouge, Y. Lemaître, A. Mathieu, Y. Morille, C. Naud, V. Noël, W. O'Hirok,
747 J. Pelon, C. Pietras, A. Protat, B. Romand, G. Scialom, and R. Vautard, 2005: SIRTa, a
748 ground-based atmospheric observatory for cloud and aerosol research. *Annales*
749 *Geophysicae*, **23**, 1–23.

750 Hadlock, R., and C. W. Kreitzberg, 1988: The Experiment on Rapidly Intensifying Cyclones
751 over the Atlantic (ERICA) field study: Objectives and plans. *Bull. Amer. Meteor. Soc.*, **69**,
752 1309-1320.

753 Harr, P. A., D. Anwender, and S. C. Jones, 2008: Predictability associated with the
754 downstream impacts of the extratropical transition of tropical cyclones: Methodology and a
755 case study of Typhoon Nabi (2005). *Mon. Wea. Rev.*, **128**, 2613–2633.

756 Harvey, B., J. Methven, and M. Ambaum, 2016: Rossby wave propagation on potential
757 vorticity fronts with finite width. *J. Fluid Mech.*, **794**, 775–797.

758 Illingworth, A.J., H.W. Barker, A. Beljaars, M. Ceccaldi, H. Chepfer, N. Clerbaux, J. Cole, J.
759 Delanoë, C. Domenech, D.P. Donovan, S. Fukuda, M. Hidakata, R.J. Hogan, A.
760 Huenerbein, P. Kollias, T. Kubota, T. Nakajima, T.Y. Nakajima, T. Nishizawa, Y. Ohno,
761 H. Okamoto, R. Oki, K. Sato, M. Satoh, M.W. Shephard, A. Velázquez-Blázquez, U.
762 Wandinger, T. Wehr, and G. van Zadelhoff, 2015: The EarthCARE Satellite: The Next
763 Step Forward in Global Measurements of Clouds, Aerosols, Precipitation, and Radiation.
764 *Bull. Amer. Meteor. Soc.*, **96**, 1311–1332.

765 Joos, H., and H. Wernli, 2012: Influence of microphysical processes on the potential vorticity
766 development in a warm conveyor belt: a case-study with the limited-area model COSMO.
767 *Quart. J. Roy. Meteor. Soc.*, **138**, 407–418.

768 Joos, H., and R. Forbes, 2016: Impact of different IFS microphysics on a warm conveyor belt
769 and the downstream flow evolution. *Quart. J. Roy. Meteor. Soc.*, **142**, 2727–2739.

770 Joly, A., K. A. Browning, P. Bessemoulin, J.-P. Cammas, G. Caniaux, J.-P. Chalon, S. A.
771 Clough, R. Dirks, K. A. Emanuel, L. Eymard, R. Gall, T. D. Hewson, P. H. Hildebrand, D.
772 Jorgensen, F. Lalauette, R. H. Langland, Y. Lemaître, P. Mascart, J. A. Moore, P. Olag.
773 Persson, F. Roux, M. A. Shapiro, C. Snyder, Z. Toth and R. M. Wakimoto, 1999:

774 Overview of the field phase of the fronts and Atlantic Storm-Track EXperiment (FASTEX)
775 project. *Quart. J. Roy. Meteor. Soc.*, **125**, 3131–3163.

776 Jones, S. C., P. A. Harr, J. Abraham, L. F. Bosart, P. J. Bowyer, J. L. Evans, D. E. Hanley, B.
777 N. Hanstrum, R. E. Hart, F. Lalaurette, M. R. Sinclair, R. K. Smith, and C. Thorncroft,
778 2003: The Extratropical Transition of Tropical Cyclones: Forecast Challenges, Current
779 Understanding, and Future Directions. *Wea. Forecasting*, **18**, 1052–1092.

780 Jones, S. C., and B. Golding, 2015: High Impact Weather Implementation Plan. Available:
781 https://www.wmo.int/pages/prog/arep/wwrp/new/high_impact_weather_project.html

782 Kew, S. F., M. Sprenger, and H. C. Davies, 2010: Potential vorticity anomalies of the
783 lowermost stratosphere: A 10-yr winter climatology. *Mon. Wea. Rev.*, **138**, 1234–1249.

784 Knippertz, P., and J. E. Martin, 2005: Tropical plumes and extreme precipitation in
785 subtropical and tropical West Africa. *Quart. J. Roy. Meteor. Soc.*, **131**, 2337–2365.

786 Krautstrunk, M., and A. Giez, 2012: The transition from FALCON to HALO era airborne
787 atmospheric research. In: *Atmospheric Physics: Background – Methods – Trends Research*
788 *Topics in Aerospace*, U. Schumann, Ed., Springer-Verlag Berlin, 604–629. Heidelberg,
789 609–624, ISBN978-3-642-30182-7.

790 Kuo, Y. H., M. A. Shapiro, and E. G. Donall, 1991: The interaction between baroclinic and
791 diabatic processes in a numerical simulation of a rapidly intensifying extratropical marine
792 cyclone. *Mon. Wea. Rev.*, **119**, 368–384.

793 Lavers, D. A., and G. Villarini, 2013: The nexus between atmospheric rivers and extreme
794 precipitation across Europe. *Geophys. Res. Lett.*, **40**, 3259–3264.

795 Madonna, E., H. Wernli, H. Joos, and O. Martius, 2014: Warm conveyor belts in the ERA-
796 Interim dataset (1979–2010). Part I: Climatology and potential vorticity evolution. *J.*
797 *Climate*, **27**, 3–26.

798 Madonna, E., M. Boettcher, C. M. Grams, H. Joos, O. Martius, and H. Wernli, 2015:
799 Verification of North Atlantic warm conveyor belt outflows in ECMWF forecasts. *Quart.*
800 *J. Roy. Meteor. Soc.*, **141**, 1333–1344.

801 Majumdar, S. J., 2016: A review of targeted observations. *Bull. Amer. Meteor. Soc.*, **97**, 2287-
802 2303.

803 Marksteiner, U., O. Reitebuch, S. Rahm, I. Nikolaus, C. Lemmerz, and B. Witschas, 2011:
804 Airborne direct-detection and coherent wind lidar measurements along the east coast of
805 Greenland in 2009 supporting ESA's Aeolus mission. *Proc. of SPIE Remote Sensing*,
806 **8182**, Prague, 19-23 September, 81810J-1 – 81820J-8.

807 Martínez-Alvarado, O., H. Joos, J. Chagnon, M. Boettcher, S. L. Gray, R. S. Plant, J.
808 Methven, and H. Wernli, 2014: The dichotomous structure of the warm conveyor belt.
809 *Quart. J. Roy. Meteor. Soc.*, **140**, 1809–1824.

810 Martínez-Alvarado, O., E. Madonna, S. L. Gray, and H. Joos, 2016: A route to systematic
811 error in forecasts of Rossby waves. *Quart. J. Roy. Meteor. Soc.*, **142**, 196–210.

812 Martius, O., E. Zenklusen, C. Schwierz, and H. C. Davies, 2006: Episodes of Alpine heavy
813 precipitation with an overlying elongated stratospheric intrusion: A climatology. *Int. J.*
814 *Climatol.*, **26**, 1149–1164.

815 Martius, O., C. Schwierz, and H. C. Davies, 2010: Tropopause-level waveguides. *J. Atmos.*
816 *Sci.*, **67**, 866–879.

817 Massacand, A. C., H. Wernli, and H. C. Davies, 2001: Influence of upstream diabatic heating
818 upon an alpine event of heavy precipitation. *Mon. Wea. Rev.*, **129**, 2822–2828.

819 Mech, M., E. Orlandi, S. Crewell, F. Ament, L. Hirsch, M. Hagen, G. Peters, and B. Stevens,
820 2014: HAMP – the microwave package on the High Altitude and LONG range research
821 aircraft (HALO). *Atmos. Meas. Tech.*, **7**, 4539–4553.

822 Methven, J., 2015: Potential vorticity in warm conveyor belt outflow. *Quart. J. Roy. Meteor.*
823 *Soc.*, **141**, 1065–1071.

824 Michel, C., and G. Rivière, 2011: A link between Rossby wave breakings and weather regime
825 transitions. *J. Atmos. Sci.*, **68**, 1730–1748.

826 Michelangeli, P., R. Vautard, and B. Legras, 1995: Weather regimes: Recurrence and quasi
827 stationarity. *J. Atmos. Sci.*, **52**, 1237–1256.

828 Nuissier, O., V. Ducrocq, D. Ricard, C. Lebeaupin, and S. Anquetin, 2008: A numerical study
829 of three catastrophic precipitating events over southern France. I: Numerical framework
830 and synoptic ingredients. *Quart. J. Roy. Meteor. Soc.*, **134**, 111–130.

831 Parsons, D.B., M. Beland, D. Burridge, P. Bougeault, G. Brunet, J. Caughey, S.M. Cavallo,
832 M. Charron, H.C. Davies, A.D. Niang, V. Ducrocq, P. Gauthier, T.M. Hamill, P.A. Harr,
833 S.C. Jones, R.H. Langland, S.J. Majumdar, B.N. Mills, M. Moncrieff, T. Nakazawa, T.
834 Paccagnella, F. Rabier, J. Redelsperger, C. Riedel, R.W. Saunders, M.A. Shapiro, R.
835 Swinbank, I. Szunyogh, C. Thorncroft, A.J. Thorpe, X. Wang, D. Waliser, H. Wernli, and
836 Z. Toth, 2017: THORPEX research and the science of prediction. *Bull. Amer. Meteor.*
837 *Soc.*, **98**, 807–830.

838 Pfahl, S., C. Schwierz, M. Croc-Maspoli, C.M. Grams, and H. Wernli, 2015: Importance of
839 latent heat release in ascending air streams for atmospheric blocking, *Nature Geosci.*, **8**,
840 610–614.

841 Pomroy, H. R., and A. J. Thorpe, 2000: The evolution and dynamical role of reduced upper-
842 tropospheric potential vorticity in intensive observing period one of FASTEX. *Mon. Wea.*
843 *Rev.*, **128**, 1817–1834.

844 Protat A., J. Pelon, J. Testud, N. Grand, P. Delville, P. Laborie, J.-P. Vinson, D. Bouniol, D.
845 Bruneau, H. Chepfer, J. Delanoe, M. Haeffelin, V. Noel, and C. Tinel, 2004: Le projet

846 RALI : Combinaison d'un radar nuage et d'un lidar pour l'étude des nuages faiblement
847 précipitants, *La Météorologie*, n° 47, 23–33.

848 Rabier F., P. Gauthier, C. Cardinali, R. Langland, M. Tsyrlunikov, A. Lorenc, P. Steinle, R.
849 Gelaro, K. Koizumi, 2008: An update on THORPEX-related research in data assimilation
850 and observing strategies. *Nonlin. Proc. Geophys.*, **15**, 81–94.

851 Rautenhaus, M., G. Bauer, and A. Dörnbrack, 2012. A web service based tool to plan
852 atmospheric research flights. *Geosci. Model Dev.*, **5**, 55–71.

853 Rautenhaus, M., M. Kern, A. Schäfler, and R. Westermann, 2015a: Three-dimensional
854 visualization of ensemble weather forecasts - Part 1: The visualization tool Met.3D
855 (version 1.0). *Geosci. Model Dev.*, **8**, 2329–2353.

856 Rautenhaus, M., C. M. Grams, A. Schäfler, and R. Westermann, 2015b: Three-dimensional
857 visualization of ensemble weather forecasts - Part 2: Forecasting warm conveyor belt
858 situations for aircraft-based field campaigns. *Geosci. Model Dev.*, **8**, 2355–2377.

859 Reitebuch, O., C. Lemmerz, E. Nagel, U. Paffrath, Y. Durand, M. Endemann, F. Fabre, and
860 M. Chaloupy, 2009: The airborne demonstrator for the direct-detection Doppler wind lidar
861 ALADIN on ADM-Aeolus: I. Instrument design and comparison to satellite instrument. *J.*
862 *Atmos. Oceanic Technol.*, **26**, 2501–2515.

863 Rex, D. F., 1950: Blocking action in the middle troposphere and its effect upon regional
864 climate. I. An aerological study of blocking action. *Tellus*, **2**, 196–211.

865 Richardson, D., J. Bidlot, L. Ferranti, A. Ghelli, T. Haiden, T. Hewson, M. Janousek, F.
866 Prates, and F. Vitart, 2012: Verification statistics and evaluations of ECMWF forecasts in
867 2011-2012. ECMWF Technical Memorandum, 688.

868 Riemer, M., and S. C. Jones, 2010: The downstream impact of tropical cyclones on a
869 developing baroclinic wave in idealized scenarios of extratropical transition. *Quart. J. Roy.*
870 *Meteor. Soc.*, **136**, 617–637.

871 Rodwell, M. J., L. Magnusson, P. Bauer, P. Bechtold, M. Bonavita, C. Cardinali, M.
872 Diamantakis, P. Earnshaw, A. Garcia-Mendez, L. Isaksen, E. Källén, D. Klocke, P. Lopez,
873 T. McNally, A. Persson, F. Prates, and N. Wedi,, 2013: Characteristics of occasional poor
874 medium-range weather forecasts for Europe. *Bull. Amer. Meteor. Soc.*, **94**, 1393–1405.

875 Schäfler, A., and F. Harnisch, 2015: Impact of the inflow moisture on the evolution of a warm
876 conveyor belt. *Quart. J. Roy. Meteor. Soc.*, **141**, 299–310.

877 Schäfler, A., M. Boettcher, C. M. Grams, M. Rautenhaus, H. Sodemann, and H. Wernli, 2014:
878 Planning of aircraft measurements within a warm conveyor belt. *Weather*, **69**, 161–166.

879 Schwierz, C., S. Dirren, and H. C. Davies, 2004: Forced waves on a zonally aligned jet
880 stream. *J. Atmos. Sci.*, **61**, 73–87.

881 Selz, T., and G. C. Craig, 2015: Upscale error growth in a high-resolution simulation of a
882 summertime weather event over Europe. *Mon. Wea. Rev.*, **143**, 813–827.

883 Sodemann, H., and A. Stohl, 2013: Moisture origin and meridional transport in Atmospheric
884 Rivers and their association with multiple cyclones, *Mon. Wea. Rev.*, **141**, 2850–2868.

885 Spensberger, C., and T. Spengler, 2014: A new look at deformation as a diagnostic for large-
886 scale flow. *J. Atmos. Sci.*, **71**, 4221–4234.

887 Sprenger, M., G. Fragkoulidis, H. Binder, M. Croci-Maspoli, P. Graf, C. M. Grams, P.
888 Knippertz, E. Madonna, S. Schemm, B. Skerlak, and H. Wernli, 2017: Global
889 climatologies of Eulerian and Lagrangian flow features based on ERA-Interim reanalyses.
890 *Bull. Amer. Meteor. Soc.*, **98**, 1739–1748.

891 Szunyogh, I., Z. Toth, R. E. Morss, S. J. Majumdar, B. J. Etherton, and C. H. Bishop, 2000:
892 The effect of targeted dropsonde observations during the 1999 Winter Storm
893 Reconnaissance Program. *Mon. Wea. Rev.*, **128**, 3520–3537.

894 Teubler, F., and M. Riemer, 2016: Dynamics of Rossby Wave Packets in a Quantitative
895 Potential Vorticity–Potential Temperature Framework. *J. Atmos. Sci.*, **73**, 1063–1081.

896 Thorpe, A. J., 2004: Weather forecasting: A centenary perspective. *Weather*, **59**, 332–335.

897 Vaughan, G., J. Methven, D. Anderson, B. Antonescu, L. Baker, T.P. Baker, S.P. Ballard,
898 K.N. Bower, P.R. Brown, J. Chagnon, T.W. Choularton, J. Chylik, P.J. Connolly, P.A.
899 Cook, R.J. Cotton, J. Crosier, C. Dearden, J.R. Dorsey, T.H. Frame, M.W. Gallagher, M.
900 Goodliff, S.L. Gray, B.J. Harvey, P. Knippertz, H.W. Lean, D. Li, G. Lloyd, O. Martínez–
901 Alvarado, J. Nicol, J. Norris, E. Öström, J. Owen, D.J. Parker, R.S. Plant, I.A. Renfrew,
902 N.M. Roberts, P. Rosenberg, A.C. Rudd, D.M. Schultz, J.P. Taylor, T. Trzeciak, R. Tubbs,
903 A.K. Vance, P.J. van Leeuwen, A. Wellpott, and A. Woolley, 2015: Cloud banding and
904 winds in intense European cyclones: results from the DIAMET project. *Bull. Amer.*
905 *Meteor. Soc.*, **96**, 249–265.

906 Weissmann, M., R. Busen, A. Dörnbrack, S. Rahm, and O. Reitebuch, 2005: Targeted
907 observations with an airborne wind lidar. *J. Atmos. Oceanic Technol.*, **22**, 1706–1719.

908 Weissmann, M., F. Harnisch, C. Wu, P. Lin, Y. Ohta, K. Yamashita, Y. Kim, E. Jeon, T.
909 Nakazawa, and S. Aberson, 2011: The Influence of Assimilating Dropsonde Data on
910 Typhoon Track and Midlatitude Forecasts. *Mon. Wea. Rev.*, **139**, 908–920.

911 Wendisch, M., D. Müller, D. Schell, and J. Heintzenberg, 2001: An air-borne spectral
912 albedometer with active horizontal stabilization. *J. Atmos. Oceanic Technol.*, **18**, 1856–
913 1866.

914 Wendisch, M., U. Pöschl, M. O. Andreae, L. A. T. Machado, R. Albrecht, H. Schlager, D.
915 Rosenfeld, S. T. Martin, A. Abdelmonem, A. Afchine, A. Araujo, P. Artaxo, H. Aufmhoff,
916 H. M. J. Barbosa, S. Borrmann, R. Braga, B. Buchholz, M. A. Cecchini, A. Costa, J.
917 Curtius, M. Dollner, M. Dorf, V. Dreiling, V. Ebert, A. Ehrlich, F. Ewald, G. Fisch, A. Fix,
918 F. Frank, D. Fütterer, C. Heckl, F. Heidelberg, T. Hüneke, E. Jäkel, E. Järvinen, T. Jurkat,
919 S. Kanter, U. Kästner, M. Kenntner, J. Kesselmeier, T. Klimach, M. Knecht, R. Kohl, T.
920 Kölling, M. Krämer, M. Krüger, T. C. Krisna, J. V. Lavric, K. Longo, C. Mahnke, A. O.
921 Manzi, B. Mayer, S. Mertes, A. Minikin, S. Molleker, S. Münch, B. Nillius, K.

922 Pfeilsticker, C. Pöhlker, A.-E. Roiger, D. Rose, D. Rosenow, D. Sauer, M. Schnaiter, J.
923 Schneider, C. Schulz, R. A. F. de Souza, A. Spanu, P. Stock, D. Vila, C. Voigt, A. Walser,
924 D. Walter, R. Weigel, B. Weinzierl, F. Werner, M. A. Yamasoe, H. Ziereis, T. Zinner, M.
925 Zöger, 2016: The ACRIDICON-CHUVA campaign: Studying tropical deep convective
926 clouds and precipitation over Amazonia using the new German research aircraft HALO.
927 *Bull. Am. Meteor. Soc.*, **97**, 10, 1885-1908.

928 Wernli, H., and H. C. Davies, 1997: A Lagrangian-based analysis of extratropical cyclones. I.
929 The method and some applications. *Quart. J. Roy. Meteor. Soc.*, **123**, 467–489.

930 Wernli, H., 1997: A Lagrangian-based analysis of extratropical cyclones. II. A detailed case-
931 study. *Quart. J. Roy. Meteor. Soc.*, **123**, 1677–1706.

932 Wernli, H., and M. Sprenger, 2007: Identification and ERA15 climatology of potential
933 vorticity streamers and cut-offs near the extratropical tropopause. *J. Atmos. Sci.*, **64**, 1569–
934 1586.

935 Wirth, M., A. Fix, P. Mahnke, H. Schwarzer, F. Schrandt, and G. Ehret, 2009: The airborne
936 multi-wavelength water vapor differential absorption lidar WALES: system design and
937 performance. *Appl. Phys. B*, **96**, 201–213.

938 Witschas, B., S. Rahm, A. Dörnbrack, J. Wagner, and M. Rapp, 2017: Airborne wind lidar
939 measurements of vertical and horizontal winds for the investigation of orographically
940 induced gravity waves. *J. Atmos. Oceanic Technol.*, **34**, 1371–1386.

941 Wulfmeyer, V., and Co-authors, 2011: The Convective and Orographically induced
942 Precipitation Study (COPS): The scientific strategy, the field phase, and research
943 highlights. *Quart. J. Roy. Meteor. Soc.*, **137**, 3–30.

944 Zhang, F., N. Bei, R. Rotunno, C. Snyder, and C. C. Epifanio, 2007: Mesoscale predictability
945 of moist baroclinic waves: Convection-permitting experiments and multistage error growth
946 dynamics. *J. Atmos. Sci.*, **64**, 3579–3594.

947 **Sidebar 1: Active remote-sensing observations for future satellite missions Aeolus and**
948 **EarthCARE.** HALO and the SAFIRE and DLR Falcon aircraft were equipped with remote-
949 sensing instruments that are specifically relevant for the future Earth Explorer satellite
950 missions EarthCARE (Illingworth et al. 2015) and Aeolus (ESA 2008) of the European Space
951 Agency (ESA). NAWDEX observations, through coordinated flights of multiple aircraft and
952 of aircraft with satellite overpasses, provide data from comparable airborne instruments for
953 the preparation and future validation of these satellite instruments.

954 HALO was equipped with the High Spectral Resolution (HSRL, 532 nm) and water vapor
955 Differential Absorption Lidar (DIAL) WALES, the HALO Microwave Package (HAMP) with
956 a 35.2 GHz cloud radar and microwave radiometers, the cloud spectrometer (specMACS) and
957 the visible to near-infrared SMART instrument (Table 2). The French Falcon was equipped
958 with the Radar-Lidar (RALI, Protat et al. 2004) payload consisting of the 94 GHz cloud radar
959 RASTA and the UV High Spectral Resolution lidar LNG (Table 2). These aircraft provide the
960 most complete instrumentation package available at the European level to mimic upcoming
961 EarthCARE measurements and thus provide valuable data for preparing the EarthCARE
962 mission and for future validation. Coordinated flights with both aircraft as well as CALIPSO-
963 Cloudsat underpasses during NAWDEX delivered independent measurements for testing
964 EarthCARE L2 algorithms at different wavelengths and for performing a first rehearsal of the
965 validation/calibration for EarthCARE.

966 Figure SB1a illustrates the complementary character of lidar and radar measurements
967 taken during the HALO research flight on 1 Oct 2016. Optically thin ice clouds at cloud top
968 are only visible in the lidar measurements (green marked curtain), while optically thicker
969 cloud regions are only visible in cloud radar measurements (red marked curtain).

970 The DLR Falcon was equipped with a Doppler wind lidar (DWL) payload consisting of
971 the A2D direct-detection DWL and a 2- μ m scanning coherent/heterodyne detection DWL.
972 The A2D is the prototype of the satellite-borne wind lidar instrument on Aeolus and provides

973 range-resolved line-of-sight wind speeds with high data coverage by exploiting both
974 molecular and particulate backscatter return. With a view to the pre-launch activities for the
975 upcoming Aeolus mission, NAWDEX offered the opportunity to extend the A2D dataset and
976 to perform wind measurements in dynamically complex scenes, including strong wind shear
977 and varying cloud conditions, as well as multiple instrument calibrations, which are a
978 prerequisite for accurate wind retrieval. RALI on board the SAFIRE Falcon complemented
979 the A2D instrument with wind measurements in clouds and aerosol-rich layers.

980 Figure SB1b shows collocated wind observations from the A2D and the 2- μm DWL from
981 a flight of the DLR Falcon east of Iceland on 4 Oct 2016. The good vertical coverage, limited
982 only by a dense cloud layer, is achieved by combining complementary information from both
983 aerosol backscatter (A2D Mie channel and 2- μm DWL) and molecular backscatter (A2D
984 Rayleigh channel).

985 **Sidebar 2: Forecast products to investigate forecast uncertainty.** NAWDEX focused on
986 weather phenomena that are poorly represented in NWP, so a strong effort to estimate forecast
987 uncertainty was essential for the planning of the IOPs. Deterministic forecasts from the
988 European Centre for Medium-Range Weather Forecasts (ECMWF), the UK Met Office, the
989 Naval Research Laboratory (NRL), Météo France, the Icelandic Meteorological Office (IMO)
990 and the Danish Meteorological Institute (DMI) were available. Additionally, ensemble
991 forecasts from the ECMWF, Met Office (MOGREPS-G) and Météo France (PEARP short-
992 range ensemble) played an essential role.

993 Each day a standard set of synoptic charts and tailored weather products (e.g. PV on
994 isentropic surfaces and WCB trajectories) were produced using a common map projection and
995 pre-defined cross sections. Ensemble diagnostics of mean and spread of several variables, as
996 well as tailored ensemble forecast products for NAWDEX-relevant features (e.g., WCB and
997 cyclone frequencies, and tropopause height) were created. These forecast products were
998 provided via web sites. In addition, an interactive web interface allowed the flight planning
999 team to compute backward and forward trajectories from planned flight tracks, facilitating the
1000 planning of flights to attempt Lagrangian re-sampling of air masses.

1001 Flight planning typically requires cross-section information, e.g., to obtain an accurate
1002 picture of tropopause height, winds speeds and cloud layers, and to assess forecast
1003 uncertainties along hypothetical flight routes. The NAWDEX community had access to
1004 special flight planning tools that allowed an interactive visualization of forecast products.
1005 Central to forecasting and flight planning operations was the "Mission Support System"
1006 (MSS; Rautenhaus et al. 2012). In addition, the interactive 3D forecast tool "Met.3D"
1007 (Rautenhaus et al. 2015a) provided specialized forecast products. Two workstations were set
1008 up at the operation center in Keflavik to run Met.3D and enable the novel ensemble
1009 forecasting workflow described in Rautenhaus et al. (2015b). Ensemble forecasts by ECMWF
1010 could be interactively analyzed in combined 2D/3D depictions. WCB trajectories and derived

1011 probabilities of WCB occurrence could be combined with additional forecast information.
1012 The ability of Met.3D to interactively navigate the ensemble data proved particularly useful,
1013 facilitating analysis of the uncertainty for features such as the predicted tropopause position.

1014 Figure SB2 shows an example of forecast products used for planning the IOP 4 flight. The
1015 +60 h deterministic IFS forecast shows ex-TS Karl as a deep surface cyclone south of
1016 Greenland (Fig. SB2a) with cyclonically wrapped PV contours resulting from an advection of
1017 low-PV air to upper levels in the outflow of a WCB (not shown). High WCB probabilities
1018 with two distinct maxima north and east of Karl indicate that the location of the tropopause
1019 and WCB outflow is predicted with high certainty (Fig. SB2b). Images from Met.3D (Fig.
1020 SB2c,d) show the relation between the jet stream, WCB and tropopause in the ECMWF
1021 ensemble mean along cross sections intersecting the waveguide and the WCB east of the
1022 surface cyclone. A cross section with ensemble mean PV (Fig. SB2c) shows a low tropopause
1023 north of the jet (depicted by an isosurface of wind speed), whereas a high tropopause appears
1024 to the south. This coincides with high probabilities of WCB (Fig. SB2d). WCB trajectories of
1025 a selected ensemble member show two distinct branches (Fig. SB2d). One branch wraps
1026 cyclonically around the cyclone and features a lower outflow compared to the second branch,
1027 which follows anticyclonic pathways at higher elevations, contributing to the elevated WCB
1028 probability maximum there. Real-time adjoint products from COAMPS (Doyle et al. 2014)
1029 were used to identify regions of initial condition sensitivity. At 12 UTC 24 Sep, the maximum
1030 moisture sensitivity is located in the low- to mid-levels and positioned along the eastern
1031 portion of TS Karl (Fig. SB2e). The adjoint sensitivity is computed using a kinetic energy
1032 response function located in a box ($450 \times 600 \text{ km}^2$ in the horizontal and extending from the
1033 surface to 700 hPa) centered on the ascending WCB at the 48 h forecast time at 12 UTC 26
1034 Sep when the IOP 4 flights were planned. Optimal perturbations derived from the adjoint
1035 sensitivity show an increase of wind speeds from 30 m s^{-1} to over 45 m s^{-1} in the WCB

1036 highlighting the importance of the mid-level moisture associated with Karl (48 h prior) for the
1037 intensification of the WCB.

Table 1: NAWDEX research aims and science goals. Region numbers refer to Fig. 1			
Aim Nr	Topic	Science Goals	Region
1	Moisture structure in the boundary layer	<ul style="list-style-type: none"> • Characterization of low-level moisture in atmospheric rivers and WCB inflow regions • Investigation of impact of low-level moisture on downstream weather evolution 	1,(2,3),4
2	Mixed phase and cirrus clouds	<ul style="list-style-type: none"> • In situ and remote sensing measurements of cloud properties and meteorological parameters during WCB ascent and outflow • Comparison of observations and models to quantify latent and radiative heating/cooling in and below WCB • Role of slantwise ascent vs. embedded convection in WCB • Characterization of vertical moisture gradient and cirrus structure in WCB outflow, and effects on radiation 	2, 3
3	Potential vorticity	<ul style="list-style-type: none"> • Quantitative estimate of PV from observations • Verification of PV structures, PV gradients and jet stream winds in numerical models • Structure of negative PV anomalies in WCB outflows and upper tropospheric ridges • Role of divergent outflow of WCBs for ridge amplification • Spatial distribution of turbulence in the free atmosphere and relationship to jet stream and PV structures 	3
4	Tropopause waveguide, predictability and consequences for HIW	<ul style="list-style-type: none"> • Relevance of amplifying small errors at tropopause level for uncertainty in surface weather downstream • Influence of observations within and outside of diabatically active regions on the predictability of downstream HIW 	3, 4
5	Instrument-driven aims	<ul style="list-style-type: none"> • Comparison of measured radiances and retrieved cloud optical properties between SMART-HALO and specMACS • Cloud regime characterization in midlatitude cyclones and analysis of model representation at different resolutions • Radiometer retrieval development for profiles and hydrometeor paths using instrument synergies • Validation of Aeolus calibration and wind retrieval algorithms • Intercomparison of wind and aerosol products from different instruments on DLR and SAFIRE Falcon • First test of EarthCARE calibration and validation strategy 	2,3

Table 2: Aircraft and instrumentation for NAWDEX and contribution to research aims (Table1)

Aircraft	Instruments	Measured and derived properties	Aim Nr
HALO	HAMP (HALO Microwave Package) Microwave radiometer with 26 channels spanning the frequency range from 22 to 183 GHz, and Ka-band (35.2 GHz) cloud radar (Mech et al. 2014)	Radiometers: Integrated water vapor, temperature and humidity profiles, liquid and ice water path Radar: profiles of radar reflectivity, depolarization ratio, vertical velocity	2,3,5
	WALES (Water Vapor Lidar Experiment in Space): Four-wavelength Differential Absorption (DIAL) and High Spectral Resolution Lidar (HSRL) (Wirth et al. 2009)	Profiles of water vapor, backscatter coefficient lidar/color ratio, particle linear depolarization ratio, particle extinction coefficient	1,2,4,5
	SMART (Spectral Modular Airborne Radiation Measurement System): Passive cloud spectrometer (Wendisch et al., 2001; Ehrlich et al., 2008)	Spectral nadir radiance, spectral upward and downward irradiance (300-2200 nm), cloud top albedo, cloud thermodynamic phase, cloud optical thickness, effective radius, cloud cover / statistics	2,4,5
	specMACS (Cloud spectrometer of the Munich Aerosol Cloud Scanner): Imaging cloud spectrometer plus 2D RGB camera (+/-35° fov) (Ewald et al. 2015)	Spectral radiance (400-2500 nm), push-broom imaging at nadir and +/- 17° across track, cloud thermodynamic phase, liquid and ice optical thickness, particle size, cloud cover	2,4,5
	Bahamas (Basic HALO Measurements and Sensor System)	In situ observations of pressure, temperature, wind, humidity, TAS aircraft position, attitude, heading, altitude	3,4,5
	Dropsondes Vaisala RD94	Temperature, humidity and wind profiles	1,2,3,4,5
DLR Falcon	A2D (ALADIN Airborne demonstrator): direct-detection DWL (Reitebuch et al. 2009, Marksteiner et al. 2011)	Profiles of line-of-sight wind speed and aerosol/cloud layers(20° off-nadir)	3,5
	2-µm scanning coherent/heterodyne detection DWL (Weissmann et al. 2005; Witschas et al. 2017)	Vertical profiles of line-of-sight wind speed, horizontal wind vectors, and aerosol/cloud layers	3,5
	Basic in situ measurements	In situ observations of pressure, temperature, wind, humidity, TAS aircraft position, attitude, heading, altitude	3,4,5
SAFIRE Falcon	RASTA (RAdar SysTem Airborne):	Doppler velocity and reflectivity from three antennas (including spectral width), cloud and	2,3,5

	95-GHz Doppler cloud radar (Delanoë et al 2013)	precipitation microphysics (ice and liquid water content), dynamics (horizontal and vertical wind)	
	LNG (Leandre New Generation): high-spectral-resolution lidar (Bruneau et al. 2015)	Three-wavelength (1064, 532, and 355 nm) backscatter lidar with polarization analysis at 355 nm, High Spectral Resolution capability including Doppler measurement, based on a Mach–Zehnder Interferometer, at 355 nm. Radiative properties and dynamics of cloud and aerosol	2,3,5
	CLIMAT infrared radiometer (Brogniez et al. 2003)	Radiances measured simultaneously in three narrowband channels centered at 8.7, 10.8, and 12.0 μm	2,4,5
	Dropsondes Vaisala RD94	Temperature, humidity and wind profiles	1,2,3,4,5
	Aircraft in situ measurements	In situ observations of pressure, temperature, wind, humidity, TAS aircraft position, attitude, heading, altitude	3,4,5
FAAM BAe 146	In situ temperature, Buck CR-2 and WVSS-2 hygrometers, two turbulence probes	Temperature, humidity, and wind and turbulent fluxes	2,3
	PCASP (aerosol size probe), CDP (scattering cloud droplet probe), CIP-15, CIP-100 (cloud imaging probes)	Cloud particle size spectrum: 2 μm -6 mm diameter, cloud droplet spectrum: 3-50 μm	2,5
	Nevzorov hot wire probe	Ice/Liquid water content	2,5
	TECO 49C UV analyser, Aerolaser AL5002, Los Gatos Fast Greenhouse Gas analyser	O ₃ , CO, CH ₄ , CO ₂	2
	Lidar: downward-pointing Leosphere ALS450 (355 nm, scattering and depolarization)	Position of different atmospheric layers below the aircraft (clear air, aerosols, cloud tops)	2
	ISMAR (International Sub-Millimetre Airborne Radiometer)	Passive radiometer with polarization and multiple channels (118, 243 (V/H), 325, 424, 448, 664 (V/H) and 874 GHz (V/H)) (IOP 11 only)	5
	MARSS (Microwave Airborne Radiometer Scanning System)	Scanning microwave radiometer operating at AMSU-B channels 16-20 (89-183GHz) and pointing both upward and downward (IOP 11 only)	5
	Dropsondes Vaisala RD94	Temperature, humidity and wind profiles	1,2,3,4,5

Table 3: IOPs, key weather systems and associated flights together with the number of dropsondes from all aircraft. As some of the long-range flights of HALO were related to different weather systems, dropsondes were assigned to the respective IOP. Aims numbered according to Table 1 show contribution to NAWDEX science goals.

IOP	Period	Key Weather systems	Date	HALO	DLR Falcon	SAFIRE Falcon	FAAM BAe 146	Drops	Aim Nr
1	16-17 Sep	Outflow of ex-TC Ian , low predictability case	17 Sep	RF01	RF01/02			10	2,3,4,5
2	21-22 Sep	WCB ascent and outflow of extratropical cyclone Ursula	21 Sep	RF02	RF03			14	2,3,4,5
3	23-25 Sep	WCB ascent of extratropical cyclone Vladiana	23 Sep	RF03	RF04		RF01 (B980)	32	1,2,3,4,5
4	22-28 Sep	Re-intensification phase of ex-TS Karl and jet streak forming downstream	26 Sep	RF04				25	2,3,4,5
			27 Sep	RF05	RF05		RF02 (B981)	22	
5	26-29 Sep	Strong WV transport of extratropical cyclone Walpurga leading to HIW in Scandinavia	27 Sep	RF05				20	1,3,4
6	1-5 Oct	Stalactite cyclone and low predictability over Europe	1 Oct	RF06		RF05		3	2,3,4,5
			2 Oct		RF07	RF06/07		9	
7	4-5 Oct	Strong extratropical cyclone originating as frontal wave near Newfoundland	4 Oct		RF08/09	RF08		5	
			5 Oct			RF09		4	2,3,4
8	6-9 Oct	TPV near Newfoundland and downstream forming cyclone	6 Oct	RF07				20	4,5
			7 Oct			RF10		7	
			9 Oct	RF08	RF10	RF11/12		9	
			10 Oct			RF13		6	
9	9-14 Oct	PV cut-off cyclone Sanchez & downstream impact over the Mediterranean	9 Oct	RF08					2,3,4,5
			10 Oct	RF09				20	
10	12-15 Oct	Formation and extension of tropopause ridge Thor and the Scandinavian anticyclone	11 Oct			RF14		4	3,4,5
			12 Oct			RF15		8	
			13 Oct	RF10		RF16		26	
			15 Oct	RF12				12	
11	14 Oct	Radar and lidar mission for instrument comparisons and satellite underflights	14 Oct	RF11		RF17/18	RF03 (B984)	15	5
12	15 Oct	TPV over Baffin Island	15 Oct	RF12					4, 5
13	18 Oct	PV streamer over UK	18 Oct	RF13	RF13/14			16	2,3
		Instrument and calibration flights	28 Sep		RF06				5
			15 Oct		RF11/12				
			16 Oct			RF19		2	
			22 Oct		RF15/16				

Table 4: NAWDEX IOPs and periods of increased ground-based observation activities.

IOP	Additional Observations	Period
1	Radiosondes from UK, Torshavn and Iceland for a temporal sequence of the arrival of outflow of ex-TC Ian as it extends northeastwards.	16-17 Sep
2	Radiosondes from UK, Iceland and eastern Greenland for a time series during arrival and passage of cyclone Ursula.	21-22 Sep
3	Radiosondes from northern UK to observe rapidly intensifying frontal cyclone Vladiana with strong WCB and ridge building.	23-25 Sep
4	Radiosondes around the northern North Atlantic and Scandinavia to observe the structure and evolution of ex-TS Karl and to observe GWs above Iceland at the jet stream. Jet streak maximum passes directly above MST radar wind profiler on South Uist, Scotland.	26-28 Sep
5	Radiosondes in UK and southern Scandinavia to observe the strong water vapor transport and related HIW. Passage of jet stream over Capel Dewi.	27-29 Sep
6	Radiosondes northwest of Iceland to observe ridge building in relation to the stalactite cyclone. Radiosondes over southern Europe to observe a cut-off downstream. Radiosondes at Iceland to observe GWs in the stratosphere.	1-5 Oct
8	Radiosondes over Iceland and eastern Greenland to observe WCB ascent and cyclone structure. Observation of orographic GWs above Iceland.	6-9 Oct
9	Radiosondes from the western Mediterranean, at Capel Dewi and at SIRTA to observe cut-off Sanchez and related HIW. Passage of outflow from Sanchez over MST radar at Capel Dewi. Radiosondes above Iceland to observe strong GW activity in the stratosphere.	10-14 Oct
8,10	Radiosondes over North Atlantic to obtain a time series of the vertical structure of ridge Thor. MST radar wind observations at Andøya, Norway.	10-15 Oct
11	Radiosondes at SIRTA to observe the downstream impact.	15-16 Oct

Table 5: NAWDEX observational highlights		
IOP	Period	Specific aspects of the observations
3	23-25 Sep	Coordinated flights to observe the cloud structure and cloud physics in the WCB ascent related to cyclone Vladiana and the interaction of the WCB outflow with the jet stream.
4	22-28 Sep	First ever observations of a TS from tropical phase and ET (SHOUT observations) through midlatitude re-intensification, jet streak formation, ridge enhancement and HIW over Scandinavia (NAWDEX observations)
5	26-29 Sep	Large-scale strong moisture transport in an atmospheric river type flow upstream of cyclone Walpurga causing HIW over Scandinavia
6	1-5 Oct	Lowest predictability case with observation of the WCB ascent and outflow of the stalactite cyclone and the subsequent influence in the onset of the European block.
8/12	26-29 Sep, 15 Oct	First ever airborne observation of temperature, wind and moisture structure of two TPV events in a phase when they interacted with the midlatitude waveguide
9	9-14 Oct	Roll-up of the positive PV filament giving rise to mesocyclone Sanchez connected to HIW in France and Italy
10	12-15 Oct	Low PV ridge builds and extends into the Arctic reinforcing the anticyclonic part of the block. Profile observations characterizing the low PV anomaly structure.
11	14 Oct	Coordination of three aircraft and joint underflight of the Calipso/Cloudsat satellite path to exploit instrument synergies of radar, lidar and radiometer instruments

1041

Table A1. Overview of the NAWDEX team members and their roles in the campaign.			
Organization	Country	Participants	Role
Monash University	Australia	Julian Quinting	Flight planning team
Environment and Climate Change Canada (ECCC)	Canada	Ron McTaggart-Cowan	PI Canadian radiosondes, science team
Division Technique, INDU	France	Frédéric Blouzon	RALI team
Institut Pierre Simon Laplace	France	Jean-Charles Dupont	Coordinator of radiosonde launches at SIRTÀ
Laboratoire d'Aérodynamique	France	Jean-Pierre Chaboureau	Flight planning team
Laboratoire de Météorologie Dynamique	France	Gwendal Rivière	Science team, flight planning team
Laboratoire Atmosphère, Milieux et Observations Spatiales France	France	Julien Delanoë Jacques Pelon	Science team, flight planning team
		Christophe Caudoux, Quitterie Cazenave, Abdenour Irbah, Mathilde Van Haecke	RALI team (airborne radar-lidar)
Météo France	France	Philippe Arbogast	Science team, flight planning team
		Jean-Marie Donier	UHF radar at Lannion
SAFIRE	France	Jean-Christophe Canonici	SAFIRE coordinator
		Dominique Duchanoy, Guillaume Seurat	Falcon pilots
		Hubert Bellec, Nelly Geil, David Mourlas, Thierry Perrin, Frédéric Pouvesle	Falcon technical support
Deutsches Zentrum für Luft- und Raumfahrt (DLR), Flight Experiments	Germany	Andreas Minikin, Robert Uebelacker, Katrin Witte	HALO and Falcon project management
		Stefan Hempe, Frank Probst	HALO and Falcon operations
		Steffen Gemsa, Michael Grossrubatscher, Stefan Grillenbeck, Philipp Weber, Roland Welser, Matthias Wiese	HALO and Falcon pilots
		Volker Dreiling, Andreas Giez, Christian Mallaun, Martin Zöger	HALO and Falcon sensor and data team
		Michael Kettenberger,	HALO technical support

		Thomas Leder, Florian Gebhardt, Christoph Grad, Stephan Storhas, David Woudsma	
Deutsches Zentrum für Luft- und Raumfahrt (DLR), Institute for Atmospheric Physics	Germany	Andreas Schäfler	Mission coordinator, science team, flight planning team
		Axel Amediek, Andreas Fix, Silke Groß, Manuel Gutleben, Martin Wirth	WALES team
		Christian Lemmerz, Oliver Lux, Uwe Marksteiner, Engelbert Nagel, Stephan Rahm, Oliver Reitebuch, Benjamin Witschas	Wind lidar team
		Florian Ewald, Martin Hagen	HAMP team
		Martina Bramberger, Alenka Senika	Radiosonde team at Keflavik, Flight planning team
Karlsruhe Institute of Technology	Germany	Pila Bossmann, Enrico Di Muzio, Florian Pantillion	Flight planning team
Max Planck Institute for Meteorology (MPI-M) Hamburg	Germany	Björn Brüggemann, David Hellmann, Lutz Hirsch, Friedhelm Jansen, Marcus Klingebiel	HAMP team
Technical University Munich	Germany	Marc Rautenhaus	Flight planning team
University of Cologne	Germany	Susanne Crewell, Lisa Dirks, Marek Jacob, Mario Mech	HAMP team
University of Hamburg, Max Planck Institute for Meteorology (MPI-M)	Germany	Felix Ament, Heike Konow	HAMP team
University of Leipzig	Germany	Tim Carlsen, André Ehrlich, Manfred Wendisch, Kevin Wolf,	SMART team
University of Mainz	Germany	Marlene Baumgart, Christian Euler, Paolo Ghinassi, Michael Riemer, Volkmar Wirth	Flight planning team
University of Munich	Germany	George Craig	HALO mission PI, science team, flight planning team
		Florian Baur, Lotte Bierdel, Christian Keil, Julia Mack, Tobias Selz	Flight planning team

		Hans Grob, Lucas Höppler, Tobias Kölling, Bernhard Mayer, Tobias Zinner	specMACS team
Norwegian Meteorological Institute	Norway	Rich Moore	NEAREX team
University of Bergen	Norway	Harald Sodemann, Thomas Spengler	NEAREX team
National Institute of Research and Development for Optoelectronics	Romania	Dragos Ene	Flight planning team
ETH Zurich	Switzerland	Heini Wernli	Science team, flight planning team
		Roman Attinger, Hanin Binder, Maxi Boettcher, Bas Crezee, Christian Grams, Jacopo Riboldi	Flight planning team
University of Bern	Switzerland	Matthias Röthlisberger	Flight planning team
Met Office	UK	Richard Cotton, Stuart Fox	FAAM aircraft
NCAS and University of Manchester	UK	Bogdan Antonescu, Hugo Ricketts, Geraint Vaughan	Capel Dewi observations, FAAM aircraft
University of Reading and NCAS	UK	Suzanne Gray, John Methven	FAAM aircraft, NAWDEX- Influence PIs, science team, flight planning team
		Ben Harvey, Jacob Maddison, Oscar Martínez-Avarado, Leo Saffin	Flight planning team
Naval Research Laboratory Monterey, CA and Washington, DC	USA	James Doyle	Science team, flight planning team
		Stephen Eckermann, Carolyn Reynolds	Flight planning team
EUMETNET		Susanne Hafner, Stefan Klink	EUMETNET coordinators
ESA		Dirk Schüttemeyer	ESA campaign section

1043 **List of Figures**

1044 **Fig. 1.** Schematic of an idealized weather situation during NAWDEX. The blue line marks
1045 the location of the waveguide with a strong isentropic PV gradient separating
1046 stratospheric (blue background, $PV > 2$ PVU) from tropospheric air (white
1047 background). The jet stream (dark blue arrows) follows the waveguide. Surface lows
1048 develop below the leading edge of upper-level positive PV anomalies (black lines
1049 indicate sea level pressure and dark blue and red lines surface cold and warm fronts,
1050 respectively). Grey shaded areas indicate clouds related to ascending WCBs (yellow
1051 arrows). Purple arrows mark divergent outflow at the tropopause. The four green
1052 boxes outline the main regions of interest, i.e., the inflow (1), ascent (2) and outflow
1053 (3) of WCBs, as well as a region of expected downstream impact (4).

1054 **Fig. 2.** Tracks of consecutively numbered research flights (RFs) of (a) HALO (97 flight
1055 hours during 13 RFs), (b) DLR Falcon (51 flight hours during 16 RFs), (c) SAFIRE
1056 Falcon (42 flight hours during 15 RFs; Flights 01 to 04 were made over France just
1057 before the campaign to calibrate the instruments), and (d) FAAM BAe 146 (15 flight
1058 hours during 3 RFs). The inset in (b) shows the DLR Falcon transfer flights and two
1059 flights to the Mediterranean at the end of the campaign.

1060 **Fig. 3.** (a) Dropsondes launched from HALO (red dots, 191 dropsondes), SAFIRE Falcon
1061 (green dots, 59 dropsondes) and FAAM BAe 146 (blue dots, 39 dropsondes). (b)
1062 Ground-based observation sites during NAWDEX: Canadian radiosonde stations
1063 (red dots), European radiosonde stations that performed only operational ascents
1064 (blue dots) and those with requested additional radiosonde launches (green dots), and
1065 six sites with additional profile observations (black diamonds).

1066 **Fig. 4.** (a-c) Synoptic-scale conditions during NAWDEX. All panels are based on ECMWF
1067 ERA-Interim data (1979-2016) and show in colors deviations of the campaign period
1068 in 2016 from the mid-September to mid-October climatology. (a-c) frequencies (all
1069 in %) of (a) surface anticyclones, (b) surface cyclones, and (c) WCB. The tracking
1070 method is explained in Sprenger et al. (2017). Black contours show the ERA-Interim
1071 37-year climatological mean; (d) best track data (HURDAT2 of the National
1072 Hurricane Center) of six tropical cyclones (red sections classified as hurricane,
1073 orange as TS and blue as extratropical storm), and cyclone tracks during the
1074 NAWDEX period (light green lines) and before/after the campaign period (dark
1075 green lines).

1076 **Fig. 5.** (a) Weather regime indices following the definition of Michel and Rivière (2011):
1077 Scandinavian blocking (blue line), positive NAO (red line), negative NAO (green
1078 line), and Atlantic ridge (yellow line), identified with a k-means clustering approach
1079 (Michelangeli et al. 1995). (b) Time series of ECMWF IFS anomaly correlation
1080 coefficient (ACC) for geopotential height at 500 hPa over an area 35 to 75°N and 60
1081 to 0°W for a forecast lead time of +120 h (shown at the initial time of the forecast):
1082 IFS deterministic forecast (black line), ensemble mean (red line), 50% of the
1083 ensemble members (orange area) and all members (yellow area). (c) NAWDEX IOPs
1084 as indicated in Table 3 (red bars). Light grey box depicts the NAWDEX campaign
1085 period and the dark grey boxes mark the duration of weather sequences as shown in
1086 Figure 6.

1087 **Fig. 6.** Three sequences that illustrate the NAWDEX storyline from trigger to interaction,
1088 development and HIW in Europe (based on ECMWF IFS operational analyses). All
1089 panels display PV on 325 K (PV < 2 PVU in white, 2 PVU \geq PV < 5 PVU in red, 5
1090 PVU \geq PV < 8 PVU in orange, PV \geq 8 PVU in yellow), contours of wind speeds
1091 (grey contours; 60, 70 and 80 m s⁻¹) and MSLP (blue contours; interval 10 hPa).
1092 Some long-lived, coherent features are labelled to enable links from one frame to the
1093 next. K refers to TS Karl; W, F, S and St mark midlatitude cyclones observed by
1094 NAWDEX; C labels a tropopause level cut-off that persists for 10 days; R1-R9 refer
1095 to the prominent ridges along the North Atlantic waveguide, identified as northward
1096 excursions of the jet stream and the isentropic PV gradient; T marks a TPV.

1097 **Fig. 7.** ECMWF IFS operational analyses of wind speed (color shading), 2 PVU (green line)
1098 at 325 K and MSLP (blue contours, in hPa) at (a) 12 UTC 23 Sep 2016 with Global
1099 Hawk flight track (black line, from 2120 UTC 22 Sep to 2100 UTC 23 Sep), (b) 12
1100 UTC 25 Sep 2016 with Global Hawk flight track (black line, from 1820 UTC 24 Sep
1101 to 1715 UTC 25 Sep), (c) 12 UTC 26 Sep 2016 with HALO flight track (black line,
1102 from 10 to 19 UTC), and (d) 12 UTC 27 Sep 2016 with HALO (black line, 1130 to
1103 2030 UTC), FAAM (pink line, 0800 to 1230 UTC) and DLR Falcon (purple line,
1104 0930 to 1330 UTC) flight tracks.

1105 **Fig. 8.** WCB observations on 23 Sep 2016 (IOP 3): (a) ECMWF IFS operational analysis of
1106 PV at 325 K (shading) and MSLP (black contours, in hPa) at 12 UTC 23 Sep 2016
1107 with HALO flight track from Iceland (gray / green line; green part corresponds to the
1108 section shown in (a) and (b)) and FAAM flight track (gray / black line; black part

1109 corresponds to track in (a) and (b)). The circle and diamond markers indicate the start
1110 and end positions of the latitudinal WCB cross-sections. (b) WALES DIAL water
1111 vapor mixing ratio (colors) and (c) HAMP radar reflectivity with HALO flight track
1112 (green line), FAAM flight track (thick black line, lowest leg was flown first) and
1113 dropsonde release positions (thin black lines). Only the part of the FAAM flight track
1114 with a spatial collocation to HALO is shown and both aircraft started at the same
1115 time, but had a time lag of ~2.5 h at the end of the last upper-most FAAM leg. (d) Ice
1116 water content as observed along the FAAM flight track. Differences between the
1117 flight tracks in (a,b) and (d) result from interpolation of FAAM position to the closest
1118 HALO observation in (a). The longitude axis in (d) was reversed to align with the
1119 time axis of the HALO flight track.

1120 **Fig. 9.** Jet stream observations on 2 Oct 2016 (IOP 6): (a) ECMWF IFS operational analysis
1121 of PV at 320 K (shading) and MSLP (black contours, in hPa), and (b) 300 hPa wind
1122 speed (colors) and geopotential height (black contours, in dam) at 06 UTC 2 Oct
1123 2016. (a) and (b) include flight tracks of the DLR Falcon (light green line) and
1124 SAFIRE Falcon (dark green line). The coordinated part of the flight from east to west
1125 shown in panels (c) and (d) is marked with the purple line. (c) DLR Falcon 2- μ m
1126 DWL wind speeds (colors) and (d) SAFIRE radar-derived wind speeds (colors).
1127 Grey area in (c) and (d) marks the topography of Greenland.

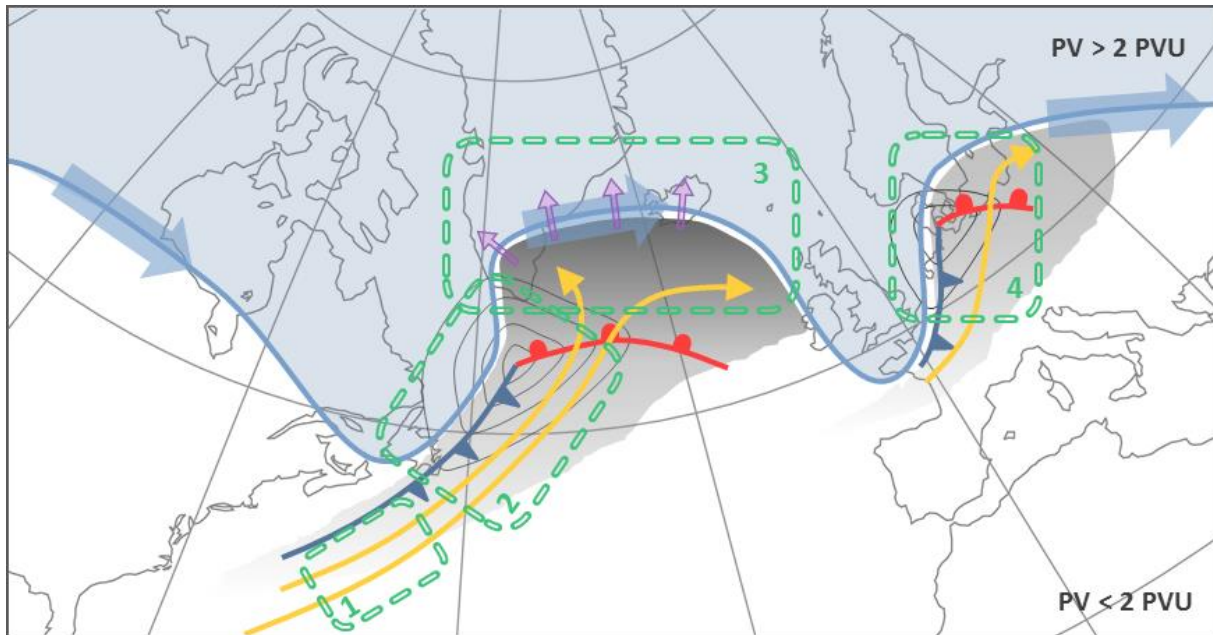
1128 **Fig.10.** (a) ERA Interim moisture fluxes at 850 hPa (arrows, shadings shows magnitude) and
1129 surface pressure (black contours, hPa) at 12 UTC 13 Oct 2016. The red star indicates
1130 the location of the SIRTA surface observation site. (b) Daily accumulated
1131 precipitation (mm) and (c) daily maximum of instantaneous surface wind in southern
1132 France on 13 Oct 2016 from the high-resolution climatological network of Météo
1133 France surface weather stations. The black areas in (b) and (c) mark topography of
1134 the French Pyrenees, the Massif Central and the French Alps. (d) Reflectivity and
1135 Doppler velocity (approximately equal to terminal fall speed) at the 25 m resolution
1136 of the radar BASTA at SIRTA on 13 Oct 2016.

1137 **Fig. SB1.** (a) Collocated observations of the vertical cloud structure below HALO, based on
1138 lidar (backscatter, along green part of the flight) and radar (radar reflectivity along
1139 red line). The underlying true color image was acquired by MODIS Aqua near the
1140 time of the flight (Global Imagery Browse Services (GIBS), operated by the
1141 NASA/GSFC/Earth Science Data and Information System). (b) Collocated wind

1142 observations on board the DLR Falcon using the A2D direct-detection wind lidar
1143 (along the blue line) and the 2- μm coherent DWL (along the red line). The latter is
1144 horizontally displaced from the actual flight track for clarity (Background picture: ©
1145 2017 Google).

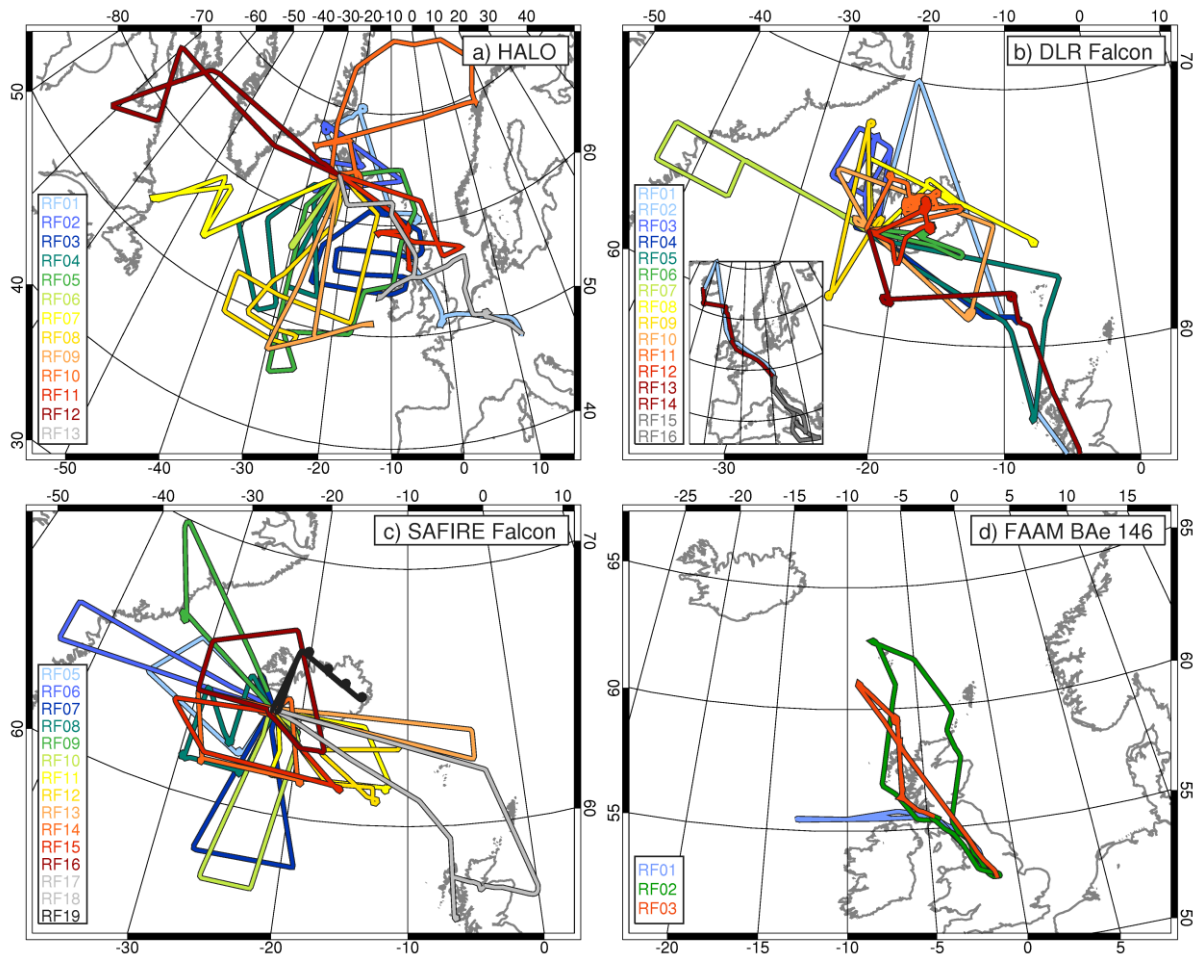
1146 **Fig. SB2.** NAWDEX forecast products for 12 UTC 26 Sep 2016 (lead time +60 h): (a)
1147 ECMWF IFS deterministic forecast of PV on 330 K (color shading) and mean sea
1148 level pressure (MSLP, in hPa). (b) WCB column probabilities of occurrence (color
1149 shading in %), derived from ECMWF ensemble (Schäfler et al. 2014; Rautenhaus et
1150 al. 2015b). Black line indicates location of cross section in Met.3D visualizations in
1151 (c) and (d). (c) Isosurface of ensemble mean wind of 60 m s^{-1} (color indicates
1152 pressure on isosurface in hPa) and MSLP (black surface contours). The cross section
1153 shows ensemble mean PV (color shading) and potential temperature (black
1154 contours). Colored lines represent WCB trajectories of ensemble member 22, starting
1155 at 06 UTC 25 Sep 2016 (colored by pressure). The black vertical poles have been
1156 added to aid spatial perception; they are labeled with pressure in hPa. (d) WCB
1157 trajectories as in (c) but from a different viewpoint and combined with a cross
1158 section showing 3D WCB probabilities (color shading, in %), ensemble mean
1159 potential temperature (black contours) and the 2 PVU isoline (red contour). (e)
1160 COAMPS adjoint 48 h forecast moisture sensitivity at 850 hPa [color shading,
1161 increments every $0.2 \text{ m}^2 \text{ s}^{-2} (\text{g kg}^{-1})^{-1}$] and 850 hPa geopotential heights (contours
1162 every 30 m) valid at 12 UTC 24 Sep (initial forecast time).

1163
1164



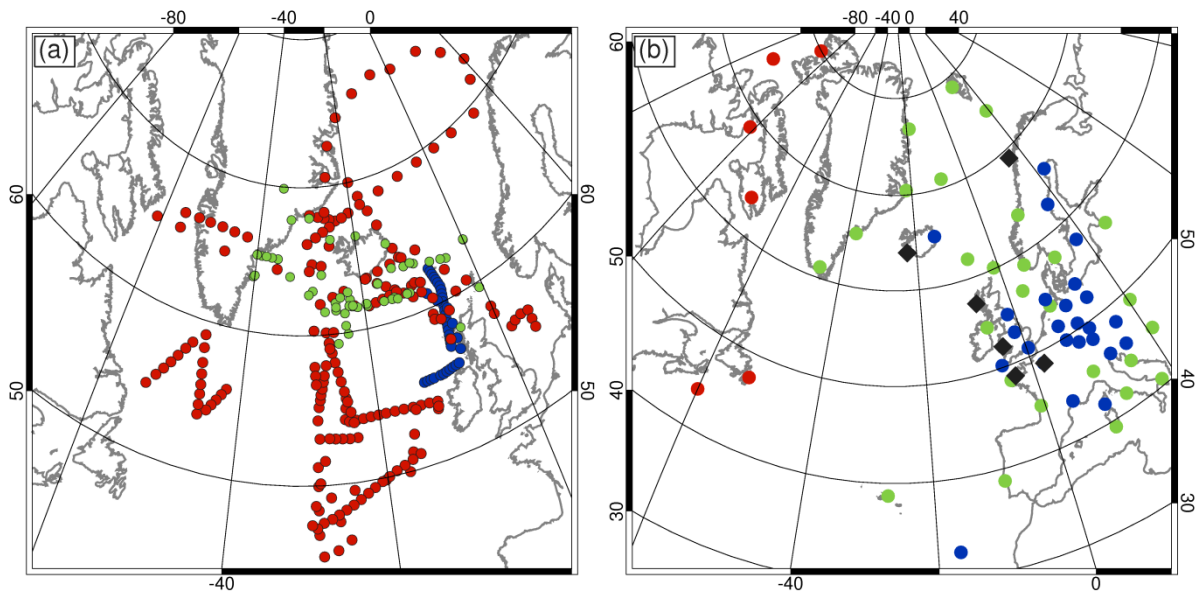
1165

1166 **Fig. 1.** Schematic of an idealized weather situation during NAWDEX. The blue line marks the
 1167 location of the waveguide with a strong isentropic PV gradient separating stratospheric (blue
 1168 background, $PV > 2$ PVU) from tropospheric air (white background). The jet stream (dark
 1169 blue arrows) follows the waveguide. Surface lows develop below the leading edge of upper-
 1170 level positive PV anomalies (black lines indicate sea level pressure and dark blue and red
 1171 lines surface cold and warm fronts, respectively). Grey shaded areas indicate clouds related to
 1172 ascending WCBs (yellow arrows). Purple arrows mark divergent outflow at the tropopause.
 1173 The four green boxes outline the main regions of interest, i.e., the inflow (1), ascent (2) and
 1174 outflow (3) of WCBs, as well as a region of expected downstream impact (4).



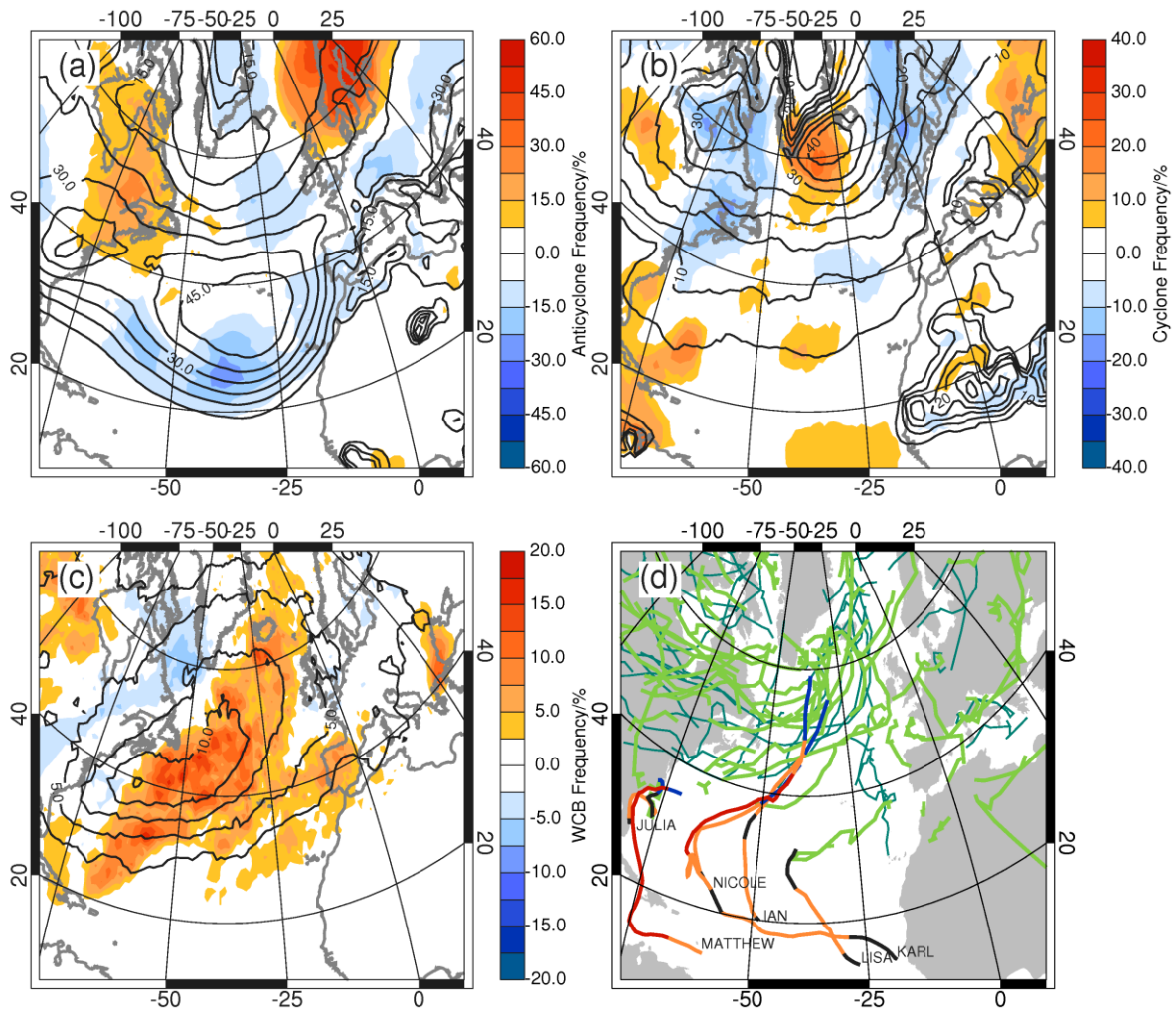
1175

1176 **Fig. 2.** Tracks of consecutively numbered research flights (RFs) of (a) HALO (97 flight hours
 1177 during 13 RFs), (b) DLR Falcon (51 flight hours during 16 RFs), (c) SAFIRE Falcon (42
 1178 flight hours during 15 RFs; Flights 01 to 04 were made over France just before the campaign
 1179 to calibrate the instruments), and (d) FAAM BAe 146 (15 flight hours during 3 RFs). The
 1180 inset in (b) shows the DLR Falcon transfer flights and two flights to the Mediterranean at the
 1181 end of the campaign.



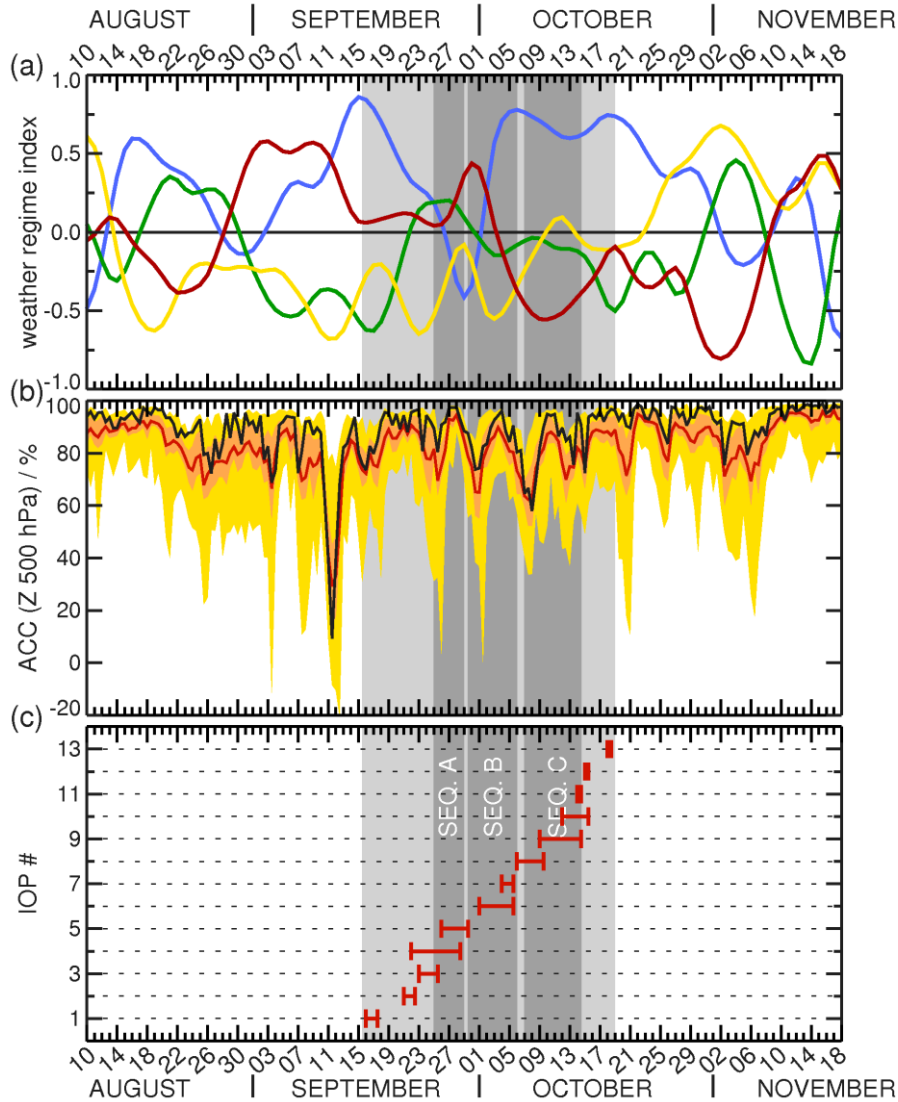
1182

1183 **Fig. 3.** (a) Dropsondes launched from HALO (red dots, 191 dropsondes), SAFIRE Falcon
 1184 (green dots, 59 dropsondes) and FAAM BAe 146 (blue dots, 39 dropsondes). (b) Ground-
 1185 based observation sites during NAWDEX: Canadian radiosonde stations (red dots), European
 1186 radiosonde stations that performed only operational ascents (blue dots) and those with
 1187 requested additional radiosonde launches (green dots), and six sites with additional profile
 1188 observations (black diamonds).

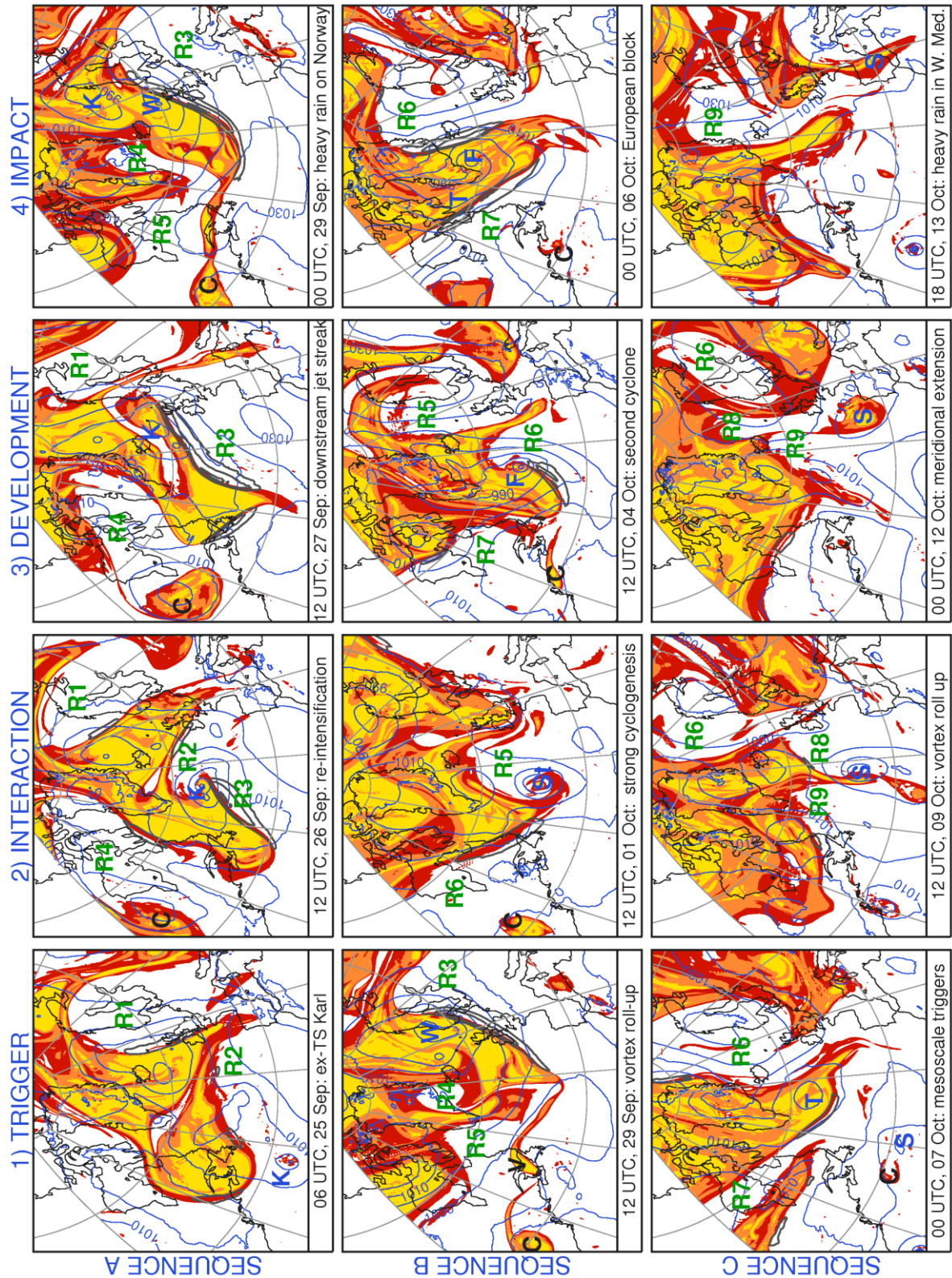


1189

1190 **Fig. 4.** (a-c) Synoptic-scale conditions during NAWDEX. All panels are based on ECMWF
 1191 ERA-Interim data (1979-2016) and show in colors deviations of the campaign period in 2016
 1192 from the mid-September to mid-October climatology. (a-c) frequencies (all in %) of (a)
 1193 surface anticyclones, (b) surface cyclones, and (c) WCB. The tracking method is explained in
 1194 Sprenger et al. (2017). Black contours show the ERA-Interim 37-year climatological mean;
 1195 (d) best track data (HURDAT2 of the National Hurricane Center) of six tropical cyclones (red
 1196 sections classified as hurricane, orange as TS and blue as extratropical storm), and cyclone
 1197 tracks during the NAWDEX period (light green lines) and before/after the campaign period
 1198 (dark green lines).



1199
 1200 **Fig. 5.** (a) Weather regime indices following the definition of Michel and Rivière (2011):
 1201 Scandinavian blocking (blue line), positive NAO (red line), negative NAO (green line), and
 1202 Atlantic ridge (yellow line), identified with a k-means clustering approach (Michelangeli et al.
 1203 1995). (b) Time series of ECMWF IFS anomaly correlation coefficient (ACC) for
 1204 geopotential height at 500 hPa over an area 35 to 75°N and 60 to 0°W for a forecast lead time
 1205 of +120 h (shown at the initial time of the forecast): IFS deterministic forecast (black line),
 1206 ensemble mean (red line), 50% of the ensemble members (orange area) and all members
 1207 (yellow area). (c) NAWDEX IOPs as indicated in Table 3 (red bars). Light grey box depicts
 1208 the NAWDEX campaign period and the dark grey boxes mark the duration of weather
 1209 sequences as shown in Figure 6.



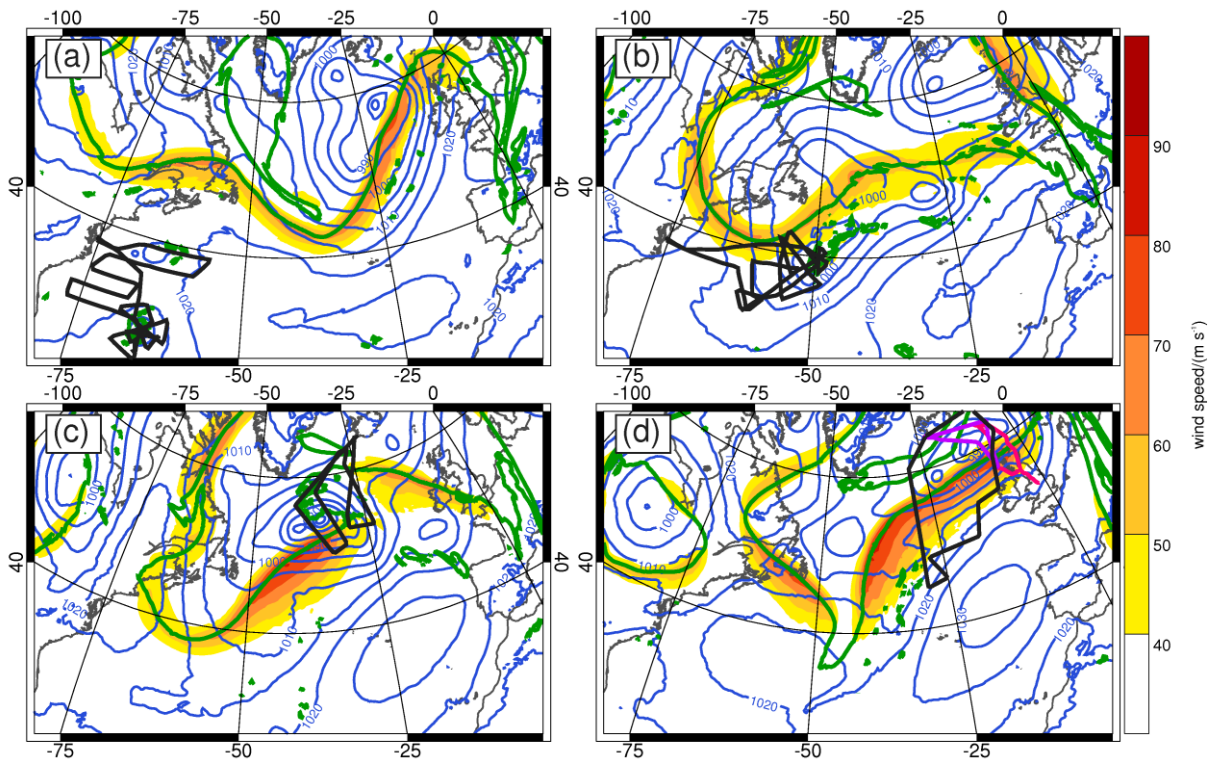
1210

1211 **Fig. 6.** Three sequences that illustrate the NAWDEX storyline from trigger to interaction,

1212 development and HIW in Europe (based on ECMWF IFS operational analyses). All panels

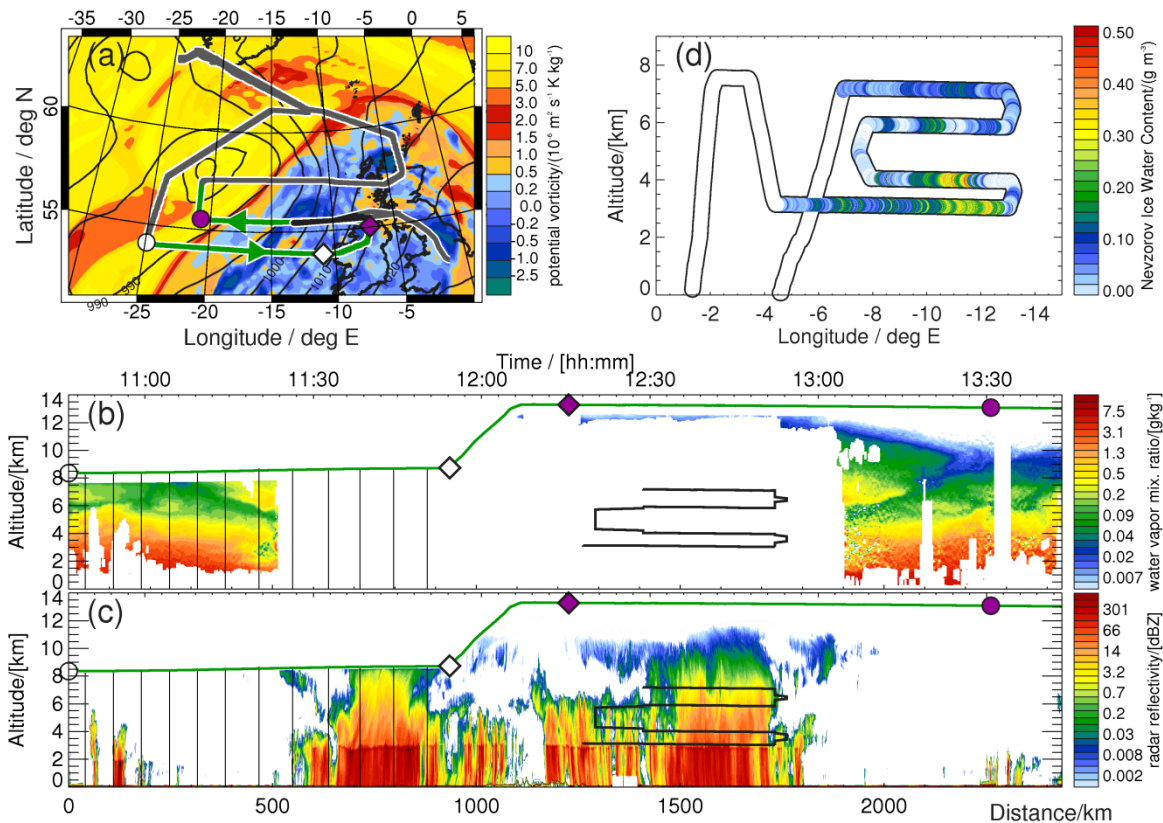
1213 display PV on 325 K (PV < 2 PVU in white, 2 PVU ≥ PV < 5 PVU in red, 5 PVU ≥ PV < 8

1214 PVU in orange, $PV \geq 8$ PVU in yellow), contours of wind speeds (grey contours; 60, 70 and
1215 80 m s^{-1}) and MSLP (blue contours; interval 10 hPa). Some long-lived, coherent features are
1216 labelled to enable links from one frame to the next. K refers to TS Karl; W, F, S and St mark
1217 midlatitude cyclones observed by NAWDEX; C labels a tropopause level cut-off that persists
1218 for 10 days; R1-R9 refer to the prominent ridges along the North Atlantic waveguide,
1219 identified as northward excursions of the jet stream and the isentropic PV gradient; T marks a
1220 TPV.



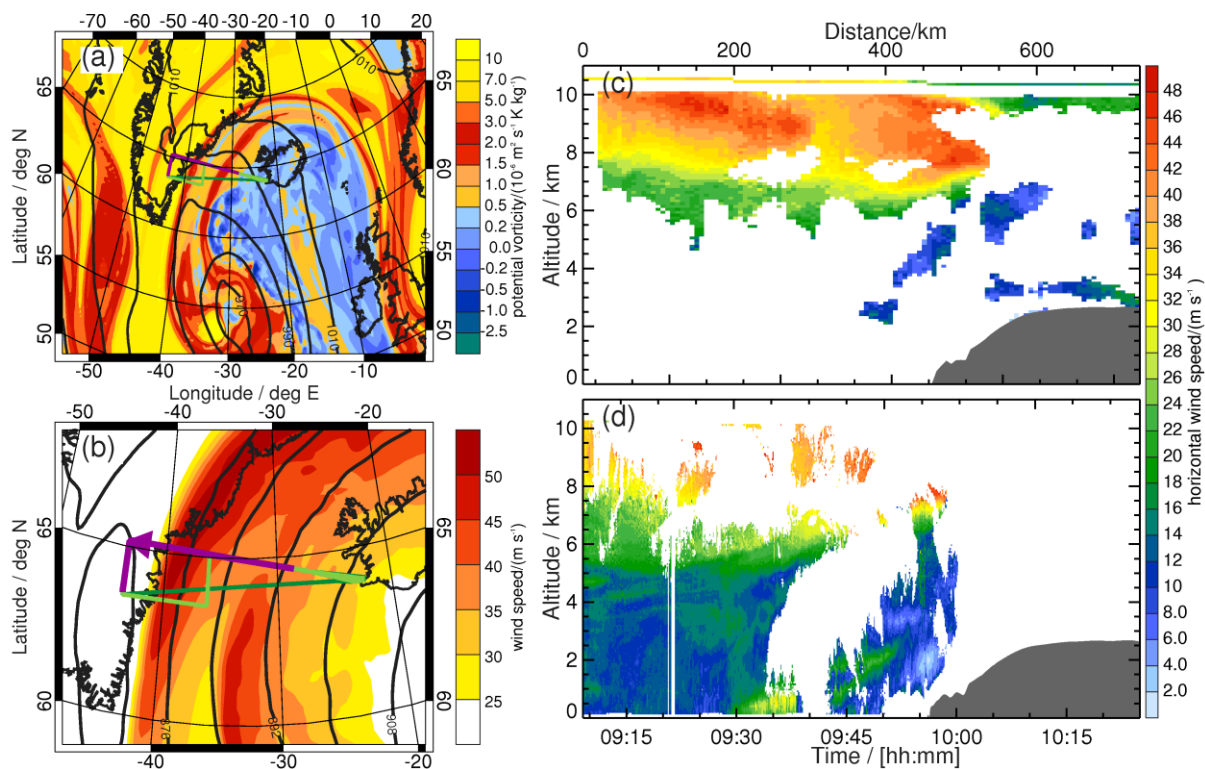
1221

1222 **Fig. 7.** ECMWF IFS operational analyses of wind speed (color shading), 2 PVU (green line)
 1223 at 325 K and MSLP (blue contours, in hPa) at (a) 12 UTC 23 Sep 2016 with Global Hawk
 1224 flight track (black line, from 2120 UTC 22 Sep to 2100 UTC 23 Sep), (b) 12 UTC 25 Sep
 1225 2016 with Global Hawk flight track (black line, from 1820 UTC 24 Sep to 1715 UTC 25
 1226 Sep), (c) 12 UTC 26 Sep 2016 with HALO flight track (black line, from 10 to 19 UTC), and
 1227 (d) 12 UTC 27 Sep 2016 with HALO (black line, 1130 to 2030 UTC), FAAM (pink line,
 1228 0800 to 1230 UTC) and DLR Falcon (purple line, 0930 to 1330 UTC) flight tracks.



1229

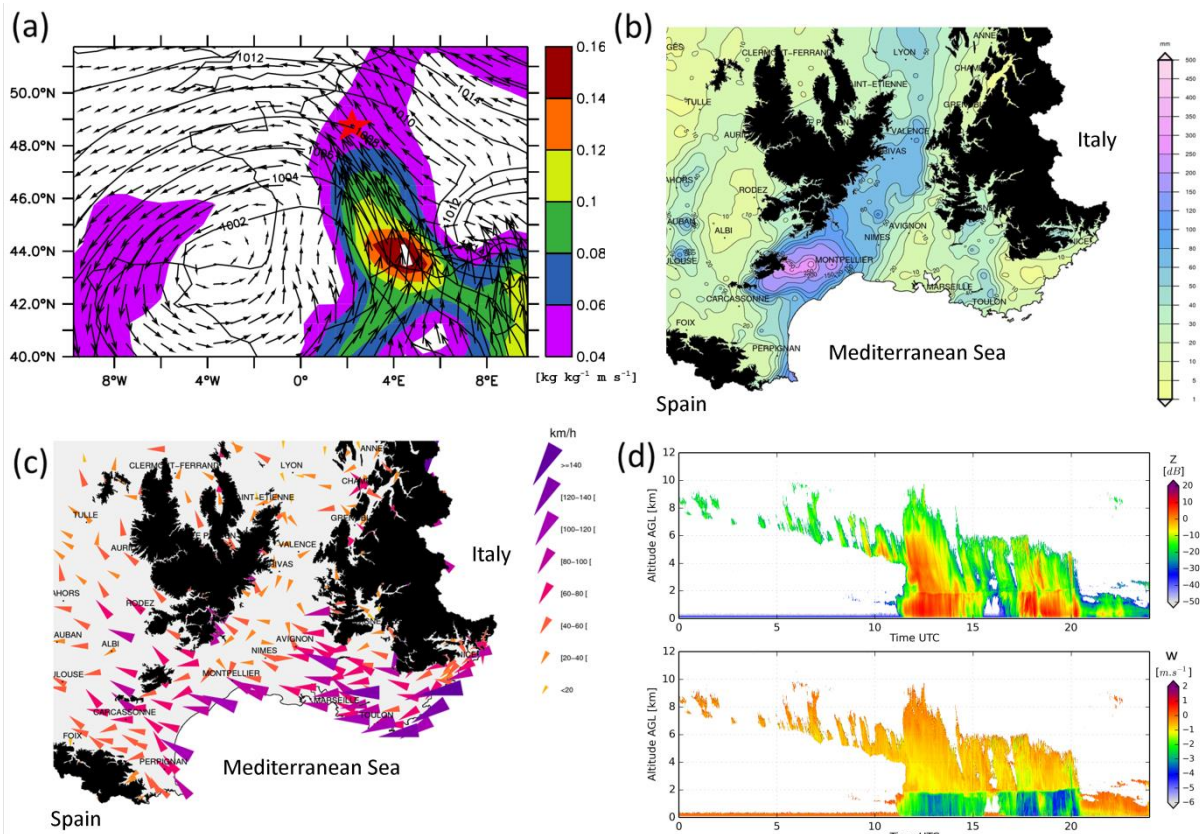
1230 **Fig. 8.** WCB observations on 23 Sep 2016 (IOP 3): (a) ECMWF IFS operational analysis of
 1231 PV at 325 K (shading) and MSLP (black contours, in hPa) at 12 UTC 23 Sep 2016 with
 1232 HALO flight track from Iceland (gray / green line; green part corresponds to the section
 1233 shown in (a) and (b)) and FAAM flight track (gray / black line; black part corresponds to
 1234 track in (a) and (b)). The circle and diamond markers indicate the start and end positions of
 1235 the latitudinal WCB cross-sections. (b) WALEs DIAL water vapor mixing ratio (colors) and
 1236 (c) HAMP radar reflectivity with HALO flight track (green line), FAAM flight track (thick
 1237 black line, lowest leg was flown first) and dropsonde release positions (thin black lines). Only
 1238 the part of the FAAM flight track with a spatial collocation to HALO is shown and both
 1239 aircraft started at the same time, but had a time lag of ~2.5 h at the end of the last upper-most
 1240 FAAM leg. (d) Ice water content as observed along the FAAM flight track. Differences
 1241 between the flight tracks in (a,b) and (d) result from interpolation of FAAM position to the
 1242 closest HALO observation in (a). The longitude axis in (d) was reversed to align with the time
 1243 axis of the HALO flight track.



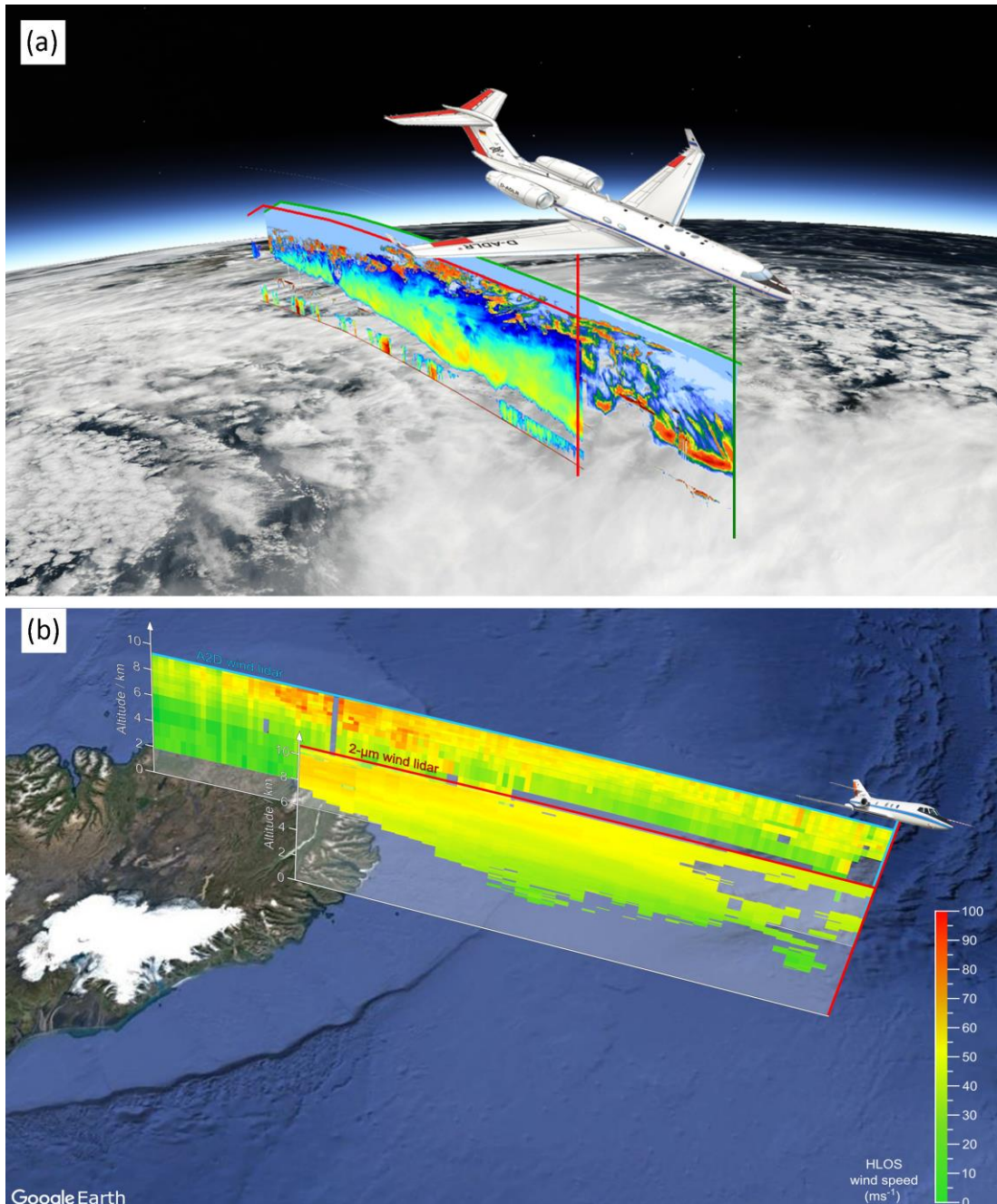
1244

1245 **Fig. 9.** Jet stream observations on 2 Oct 2016 (IOP 6): (a) ECMWF IFS operational analysis
 1246 of PV at 320 K (shading) and MSLP (black contours, in hPa), and (b) 300 hPa wind speed
 1247 (colors) and geopotential height (black contours, in dam) at 06 UTC 2 Oct 2016. (a) and (b)
 1248 include flight tracks of the DLR Falcon (light green line) and SAFIRE Falcon (dark green
 1249 line). The coordinated part of the flight from east to west shown in panels (c) and (d) is
 1250 marked with the purple line. (c) DLR Falcon 2- μm DWL wind speeds (colors) and (d)
 1251 SAFIRE radar-derived wind speeds (colors). Grey area in (c) and (d) marks the topography of
 1252 Greenland.

1253



1254
 1255 **Fig.10.** (a) ERA Interim moisture fluxes at 850 hPa (arrows, shadings shows magnitude) and
 1256 surface pressure (black contours, hPa) at 12 UTC 13 Oct 2016. The red star indicates the
 1257 location of the SIRT A surface observation site. (b) Daily accumulated precipitation (mm) and
 1258 (c) daily maximum of instantaneous surface wind in southern France on 13 Oct 2016 from the
 1259 high-resolution climatological network of Météo France surface weather stations. The black
 1260 areas in (b) and (c) mark topography of the French Pyrenees, the Massif Central and the
 1261 French Alps. (d) Reflectivity and Doppler velocity (approximately equal to terminal fall
 1262 speed) at the 25 m resolution of the radar BASTA at SIRT A on 13 Oct 2016.



1263

1264 **Fig. SB1.** (a) Collocated observations of the vertical cloud structure below HALO, based on

1265 lidar (backscatter, along green part of the flight) and radar (radar reflectivity along red line).

1266 The underlying true color image was acquired by MODIS Aqua near the time of the flight

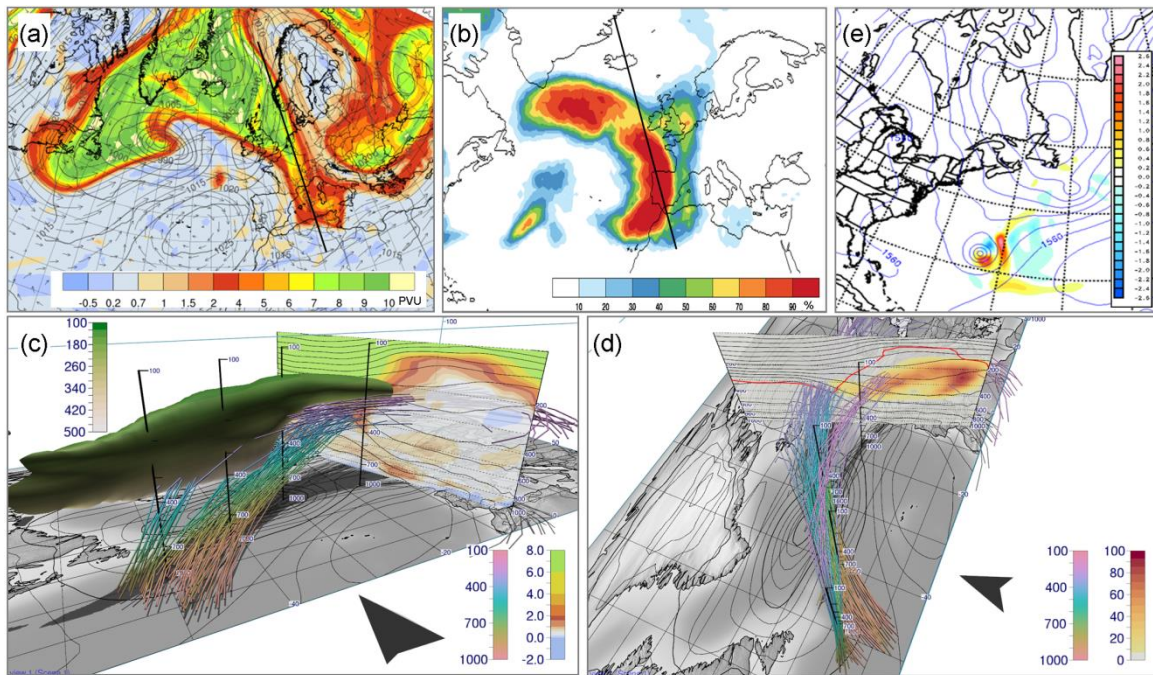
1267 (Global Imagery Browse Services (GIBS), operated by the NASA/GSFC/Earth Science Data

1268 and Information System). (b) Collocated wind observations on board the DLR Falcon using

1269 the A2D direct-detection wind lidar (along the blue line) and the 2- μ m coherent DWL (along

1270 the red line). The latter is horizontally displaced from the actual flight track for clarity

1271 (Background picture: © 2017 Google).



1272

1273 **Fig. SB2.** NAWDEX forecast products for 12 UTC 26 Sep 2016 (lead time +60 h): (a)
 1274 ECMWF IFS deterministic forecast of PV on 330 K (color shading) and mean sea level
 1275 pressure (MSLP, in hPa). (b) WCB column probabilities of occurrence (color shading in %),
 1276 derived from ECMWF ensemble (Schäfler et al. 2014; Rautenhaus et al. 2015b). Black line
 1277 indicates location of cross section in Met.3D visualizations in (c) and (d). (c) Isosurface of
 1278 ensemble mean wind of 60 m s^{-1} (color indicates pressure on isosurface in hPa) and MSLP
 1279 (black surface contours). The cross section shows ensemble mean PV (color shading) and
 1280 potential temperature (black contours). Colored lines represent WCB trajectories of ensemble
 1281 member 22, starting at 06 UTC 25 Sep 2016 (colored by pressure). The black vertical poles
 1282 have been added to aid spatial perception; they are labeled with pressure in hPa. (d) WCB
 1283 trajectories as in (c) but from a different viewpoint and combined with a cross section
 1284 showing 3D WCB probabilities (color shading, in %), ensemble mean potential temperature
 1285 (black contours) and the 2 PVU isoline (red contour). (e) COAMPS adjoint 48 h forecast
 1286 moisture sensitivity at 850 hPa [color shading, increments every $0.2 \text{ m}^2 \text{ s}^{-2} (\text{g kg}^{-1})^{-1}$] and 850
 1287 hPa geopotential heights (contours every 30 m) valid at 12 UTC 24 Sep (initial forecast time).